J. Fluid Mech. (2025), *vol*. 1002, A42, doi:10.1017/jfm.2024.1193

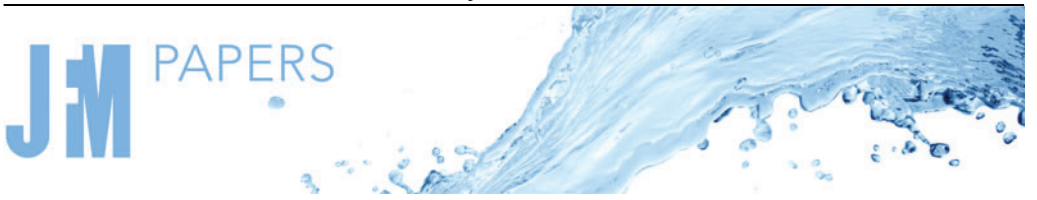

Mode-to-mode nonlinear energy transfer in turbulent channel flows

Jitong Ding[1],†, **Daniel Chung**[1] **and Simon J. Illingworth**[1]

[1]Department of Mechanical Engineering, University of Melbourne, Victoria 3010, Australia

(Received 8 July 2024; revised 6 December 2024; accepted 9 December 2024)

We investigate nonlinear energy transfer for channel flows at friction Reynolds numbers $Re_\tau = 180$ and 590. The key feature of the analysis is that we quantify the energy transferred from a source mode to a recipient mode, with each mode characterised by a streamwise wavenumber and a spanwise wavenumber. This is achieved through an explicit examination of the triadic interactions of the nonlinear energy transfer term in the spectral turbulent kinetic energy equation. First, we quantify the nonlinear energy transfer gain and loss for individual Fourier modes. The gain and loss cannot be obtained without expanding the nonlinear triadic interactions. Second, we quantify the nonlinear energy transfer budgets for three types of modes. Each type of mode is characterised by a specific region in streamwise–spanwise wavenumber space. We find that a transverse cascade from streamwise-elongated modes to spanwise-elongated modes exists for all three types of modes. Third, we quantify the forward and inverse cascades between resolved scales and subgrid scales in the spirit of large-eddy simulations. For the cutoff wavelength range that we consider, the forward and inverse cascades between the resolved scales and subgrid scales result in a net forward cascade from the resolved scales to the subgrid scales. The shape of the net forward cascade curve with respect to the cutoff wavelength resembles the net forward cascade predicted by the Smagorinsky eddy viscosity.

Key words: turbulence theory, turbulence modelling

1. Introduction

Turbulence involves energy transfer across a wide range of scales and is important for many applications, such as combustion (Ertesvåg & Magnussen 2000), ocean engineering (Hasselmann, Munk & MacDonald 1963) and the Earth's climate (Richardson 1922). It is generally understood that energy is transferred from large scales to small scales,

† Email address for correspondence: jitongd@student.unimelb.edu.au

known as the forward cascade (Richardson 1922; Kolmogorov 1941). But an inverse cascade in which energy is transferred from small scales to large scales also occurs (Domaradzki *et al.* 1994; Dunn & Morrison 2003; Cimarelli, De Angelis & Casciola 2013; Cimarelli *et al.* 2016). Both forward and inverse cascades are involved in vortex regeneration in the self-sustaining process for wall turbulence (Hamilton, Kim & Waleffe 1995; Waleffe 1997). In turbulence modelling and simulation, failure to consider backscatter can result in inaccurate large-eddy simulations (LES) (Piomelli *et al.* 1991; Härtel *et al.* 1994; Cimarelli & De Angelis 2014). The above considerations are all dictated by the physics of the energy cascade across scales in wall-bounded turbulent flows.

This energy cascade can be viewed in either physical space or Fourier space. In physical space, the energy cascade is characterised by high spatio-temporal intermittency (Meneveau & Sreenivasan 1991). In Fourier space, for flow geometries (such as channels, pipes, boundary layers) with at least one homogeneous spatial dimension, the energy cascade can be interpreted as energy redistributed among different Fourier modes, described by the nonlinear energy transfer term in the spectral turbulent kinetic energy (sTKE) equation (Tennekes & Lumley 1972; Pope 2000). Here, a mode refers to scales with a particular wavelength in the homogeneous direction. The nonlinear energy transfer term in the spectral energy budget represents the net energy received by a particular mode from all other modes through nonlinear interactions since the term is a convolution of all wavenumber-compatible triadic interactions. Triadic interaction refers to the energy transfer among three modes whose wavenumbers satisfy $\boldsymbol{k}+\boldsymbol{p}+\boldsymbol{q}=\boldsymbol{0}$ (Domaradzki & Rogallo 1990; Domaradzki 1992; Waleffe 1992; Domaradzki *et al.* 1994). However, we merely know the net energy transfer for each Fourier mode, not the detailed contributions to this net value from the nonlinear energy transfer term, because the convolution hides the individual triadic interactions.

Compared to homogeneous isotropic turbulence, only a few studies have explored the triadic interactions of nonlinear energy transfer for channel flows (Domaradzki *et al.* 1994; Webber, Handler & Sirovich 2002; Cho, Hwang & Choi 2018; Karban *et al.* 2023). A single wavenumber triad could be interpreted as energy transfer from a source mode to a recipient mode via an advective mode (Domaradzki & Rogallo 1990; Smyth 1992; Webber *et al.* 2002; Alexakis, Mininni & Pouquet 2005; Jin, Symon & Illingworth 2021). To gain more insight into the energy cascade in channel flows, we expand the convolution of the nonlinear energy transfer term in streamwise–spanwise wavenumber space. Following this, we formulate a variable $\hat{M}_{(s_x,s_y)(k_x,k_y)}$ (defined in § 2.3) that represents mode-to-mode nonlinear energy transfer in streamwise–spanwise wavenumber space. Compared to the convolution term, which gives us only the net energy transfer for a specific Fourier mode, with this variable, we are able to quantify the energy transfer between any two Fourier modes.

We use this four-dimensional variable $\hat{M}_{(s_x,s_y)(k_x,k_y)}$ (one source mode and one recipient mode, with each mode consisting of a streamwise wavenumber and a spanwise wavenumber) to explore three things using direct numerical simulations (DNS) datasets at $Re_\tau = 180$ and 590. First, since the nonlinear energy transfer term in the sTKE equations could give us only one value representing the net energy transfer for each mode previously, we use this new variable $\hat{M}_{(s_x,s_y)(k_x,k_y)}$ to obtain two additional values quantifying the net energy transfer gain and loss due to nonlinear interactions for each mode. Second, we investigate the nonlinear energy transfer budgets for three types of modes. Similar to Jovanović & Bamieh (2005), each type of mode indicates a specific region in the streamwise–spanwise wavenumber space. Third, we apply a cutoff wavenumber filter to divide all the scales in the DNS into large and small scales. In the spirit of LES, the large

scales are treated as resolved scales, while the small scales are treated as subgrid scales. We quantify the forward cascade and inverse cascade between resolved and subgrid scales. We further compare the net forward cascade calculated using $\hat{M}$ with the forward cascade calculated using the Smagorinsky eddy viscosity. The similarities and differences between $Re_\tau = 180$ and 590 are discussed. It is worth noting that we integrate energy transfer in the wall-normal direction and over time to obtain $\hat{M}$. Although $\hat{M}$ provides information in the streamwise–spanwise wavenumber space, it does not capture wall-normal-dependent and time-dependent information.

This paper is organised as follows. In § 2, the equations for the sTKE budget and variable $\hat{M}_{(s_x,s_y)(k_x,k_y)}$ representing mode-to-mode nonlinear energy transfer are derived. The DNS datasets are described in § 3. Section 4 presents the results. Specifically, § 4.1 revisits the previous study from Symon, Illingworth & Marusic (2021) about the wall-normal integrated spectral energy transfer budget; § 4.2 uses two examples to interpret variable $\hat{M}$ and to illustrate energy transfer pathways; § 4.3 presents the positive and negative nonlinear energy transfer spectra; § 4.4 investigates the nonlinear energy transfer for three types of modes; and § 4.5 quantifies the forward cascade and inverse cascade between resolved scales and subgrid scales in the spirit of LES. Conclusions are drawn in § 5.

2. Methods

In § 2.1, we describe the governing equations for plane Poiseuille flow and their non-dimensionalisation. Then an introduction to the sTKE equation integrated across the channel height is presented in § 2.2. In § 2.3, we introduce a four-dimensional variable quantifying mode-to-mode nonlinear energy transfer and the pertinent properties.

2.1. *Plane Poiseuille flow equations*

Consider the non-dimensional incompressible Navier–Stokes equations for the fluctuation velocities after a decomposition $\mathcal{U}_i = U_i + u_i$, where $\mathcal{U}_i$, U_i and u_i represent the instantaneous velocity, streamwise–spanwise-averaged velocity and fluctuation velocity, respectively:

$$\left.\begin{aligned} \frac{\partial u_i}{\partial x_i} &= 0, \\ \frac{\partial u_i}{\partial t} + u_j \frac{\partial U_i}{\partial x_j} + U_j \frac{\partial u_i}{\partial x_j} + \frac{\partial}{\partial x_j}(u_i u_j - \langle u_i u_j \rangle_{xy}) &= -\frac{\partial p}{\partial x_i} + \frac{1}{Re_\tau} \frac{\partial^2 u_i}{\partial x_j \partial x_j}, \end{aligned}\right\} \tag{2.1}$$

where the indices $i = 1, 2, 3$ represent the x (streamwise), y (spanwise) and z (wall-normal) directions. The corresponding velocity components are denoted by u, v and w. Pressure is denoted as p. Velocity scales are non-dimensionalised using the friction velocity u_τ, length scales are non-dimensionalised using the channel half-height h, time scales are non-dimensionalised using h/u_τ, and pressure is non-dimensionalised using ρu_τ^2, where $u_\tau = \sqrt{\tau_w/\rho}$, ρ is the density, τ_w is the mean wall shear stress, and u_τ is the friction velocity. Then the friction Reynolds number $Re_\tau = h u_\tau / \nu$ is defined using h, u_τ and the kinematic viscosity ν. Here, $\langle\,\rangle_{xy}$ means averaging in the streamwise and spanwise directions.

2.2. *Spectral energy transfer budget*

Owing to the periodic assumption in the streamwise and spanwise directions, we investigate energy transfer in two-dimensional streamwise–spanwise wavenumber space. We define the inner product $\langle c_1, c_2\rangle = \frac{1}{2}\int_{-1}^{1} c_1^* c_2 \,\mathrm{d}z$, where c_1 and c_2 are two complex vectors, and * denotes the complex conjugate. We use this inner product definition to represent the wall-normal integrated kinetic energy at mode (k_x, k_y) (Reddy & Henningson 1993; Domaradzki *et al.* 1994):

$$\hat{E}(k_x, k_y) = \tfrac{1}{2}\langle \hat{u}^{(k_x,k_y)}, \hat{u}^{(k_x,k_y)}\rangle + \tfrac{1}{2}\langle \hat{v}^{(k_x,k_y)}, \hat{v}^{(k_x,k_y)}\rangle + \tfrac{1}{2}\langle \hat{w}^{(k_x,k_y)}, \hat{w}^{(k_x,k_y)}\rangle, \tag{2.2}$$

where k_x is the streamwise wavenumber, and k_y is the spanwise wavenumber. The wavenumber is defined as $k = 2\pi/\lambda$, where λ is the wavelength. According to the non-dimensionalisation rule, wavenumbers k_x and k_y are scaled with the channel height h. Wavenumbers in viscous units are sometimes used: $k^+ = kv/hu_\tau$. The superscript refers to the individual Fourier mode under consideration: $\hat{u}^{(k_x,k_y)}$ is the Fourier coefficient of u at wavenumber (k_x, k_y).

The spectral energy transfer budget can be obtained by first taking Fourier transforms of (2.1) in the x and y directions, and then multiplying by the conjugate mode $(\hat{u}_i^{(k_x,k_y)})^* = \hat{u}_i^{(-k_x,-k_y)}$. Then we integrate the energy transfer budget in the wall-normal direction and obtain (Symon *et al.* 2021)

$$\overline{\frac{\partial \hat{E}(k_x,k_y)}{\partial t}} = \underbrace{-\overline{\left\langle \hat{u}, \frac{\mathrm{d}U}{\mathrm{d}z}\hat{w}\right\rangle}}_{\hat{P}(k_x,k_y)} \underbrace{-\frac{1}{Re_\tau}\overline{\left\langle \frac{\widehat{\partial u_i}}{\partial x_j}, \frac{\widehat{\partial u_i}}{\partial x_j}\right\rangle}}_{\hat{D}(k_x,k_y)} \underbrace{-\overline{\left\langle \hat{u}_i, \frac{\widehat{\partial u_i u_j}}{\partial x_j}\right\rangle}}_{\hat{N}(k_x,k_y)}, \tag{2.3a}$$

$$\hat{P}(k_x,k_y) - \hat{D}(k_x,k_y) + \hat{N}(k_x,k_y) = 0, \tag{2.3b}$$

with summation implied in the coordinate directions over the repeating index i or j. The angle brackets denote the inner product definition provided at the beginning of this section. This inner product involves integration in the wall-normal direction. The overbar denotes time-averaging. Equation (2.3*a*) describes the wall-normal integrated energy transfer balance for a single Fourier mode. The left-hand side is the time derivative of the turbulent kinetic energy for a single Fourier mode; $\hat{P}$ represents production, $-\hat{D}$ represents (pseudo) dissipation (Pope 2000), and $\hat{N}$ represents the net nonlinear energy transfer (the net energy that mode (k_x, k_y) receives through nonlinear interactions with all other modes). The size of an eddy corresponding to a given Fourier mode can be defined using the isotropic wall-parallel wavelength: $\lambda_I = 2\pi/k_I$, where $k_I^2 = k_x^2 + k_y^2$ (Jiménez 2018; Lee & Moser 2019). For a statistically stationary flow, the left-hand side of (2.3*a*) is zero, meaning that the wall-normal integrated production, dissipation and net nonlinear energy transfer reach a balance for each mode, as shown in (2.3*b*). According to the normalisation described in § 2.1, the energy transfer terms ($\hat{P}$, $\hat{D}$ and $\hat{N}$ in (2.3*a*)) are non-dimensionalised by u_τ^3/h. Strictly speaking, production, dissipation and nonlinear energy transfer in (2.3*a*) are energy transfer rates because it is the kinetic energy variation rate on the left-hand side of (2.3*a*).

Throughout this paper, we use non-negative wavenumbers to describe a mode (k_x, k_y), where $k_x \geq 0$ and $k_y \geq 0$. Energy transfer at mode $(0, 0)$ is zero because of the chosen decomposition of the velocities. The energy transfer at mode (k_x, k_y) with $k_x > 0$ and $k_y > 0$ contains the contributions from the wavenumber pairs (k_x, k_y), $(-k_x, -k_y)$, $(-k_x, k_y)$ and

$(k_x, -k_y)$. For example, production at mode (k_x, k_y) is equal to $\hat{P}(k_x, k_y) + \hat{P}(-k_x, k_y) +$ c.c., where c.c. represents complex conjugate terms. The energy transfer at mode $(k_x, 0)$ with $k_x > 0$ contains the contributions from the wavenumber pairs $(k_x, 0)$ and $(-k_x, 0)$. For example, production at mode $(k_x, 0)$ is equal to $\hat{P}(k_x, 0) +$ c.c.. The energy transfer at mode $(0, k_y)$ with $k_y > 0$ contains the contributions from the wavenumber pairs $(0, k_y)$ and $(0, -k_y)$. For example, production at mode $(0, k_y)$ is equal to $\hat{P}(0, k_y) +$ c.c.. Following this, the energy transfer terms $\hat{P}, \hat{D}, \hat{N}$ for each mode (k_x, k_y) with $k_x \geq 0$, $k_y \geq 0$ are real numbers. The derivation of (2.3*a*) can be found in Pope (2000).

In (2.3*a*), $\hat{N}(k_x, k_y)$ is conservative:

$$\int_0^\infty \int_0^\infty \hat{N}(k_x, k_y)\, \mathrm{d}k_x\, \mathrm{d}k_y = 0. \tag{2.4}$$

Equation (2.4) states that the sum of the net nonlinear energy transfer across all Fourier modes is zero. This implies that nonlinear energy transfer redistributes energy across scales without adding or removing energy overall. This can also be seen from the Reynolds–Orr equation: the only energy source for turbulence is production, and the only energy sink for turbulence is dissipation (Schmid & Henningson 2001).

2.3. *Mode-to-mode nonlinear energy transfer* $\hat{M}_{(s_x,s_y)(k_x,k_y)}$

On the right-hand side of (2.3*a*), $\hat{N}(k_x, k_y)$ represents the net energy received by mode (k_x, k_y) from nonlinear interactions between mode (k_x, k_y) and all other modes, without giving information about the individual contributions to this net value. To illustrate, mode (k_x, k_y) could potentially gain energy from mode (s_{x1}, s_{y1}), lose energy to mode (s_{x2}, s_{y2}), gain energy from mode (s_{x3}, s_{y3}), lose energy to mode (s_{x4}, s_{y4}), and so on. But those mode-to-mode nonlinear energy transfers are hidden because $\hat{N}$ represents a sum over all modes.

In (2.3*a*), $\hat{N}(k_x, k_y)$ can be expressed as a convolution composed of all wavenumber-compatible triadic interactions:

$$\hat{N}(k_x, k_y) = \int_0^\infty \int_0^\infty \hat{M}_{(s_x,s_y)(k_x,k_y)}\, \mathrm{d}s_x\, \mathrm{d}s_y, \tag{2.5}$$

where

$$\hat{M}_{(s_x,s_y)(k_x,k_y)} = -\overline{\hat{u}_i^{(-k_x,-k_y)}\, \hat{u}_j^{(k_x-s_x,k_y-s_y)}\, \widehat{\frac{\partial u_i}{\partial x_j}}^{(s_x,s_y)}}. \tag{2.6}$$

A single set of triadic interactions involving three distinct modes can be understood as the energy transferred nonlinearly from a source mode (s_x, s_y) to a recipient mode (k_x, k_y) with the help of an advective mode $(k_x - s_x, k_y - s_y)$ (Domaradzki & Rogallo 1990; Smyth 1992; Webber *et al.* 2002; Alexakis *et al.* 2005; Jin *et al.* 2021; de Salis Young, Hao & Garcia-Mayoral 2024). Here, s_x is the streamwise wavenumber and s_y is the spanwise wavenumber for another mode (s_x, s_y) different from mode (k_x, k_y). Thus the four-dimensional variable $\hat{M}_{(s_x,s_y)(k_x,k_y)}$ describes the energy transferred nonlinearly from one Fourier mode (s_x, s_y) to another Fourier mode (k_x, k_y). Compared to $\hat{N}$, $\hat{M}$ provides more detailed information about nonlinear energy transfer. However, it should be noted that $\hat{M}$ does not capture all details as $\hat{M}$ measures the time-averaged wall-normal-integrated energy transfer, condensing the information in the wall-normal direction and over time.

Re_τ	L_x	L_y	$n_x \times n_y \times n_z$	Δx^+	Δy^+	Δz^+_{max}	Δz^+_{min}	Δt^+
180	2π	π	$112 \times 112 \times 150$	10.00	5.05	3.77	0.04	0.36
590	2π	π	$384 \times 384 \times 500$	9.65	4.83	3.71	0.01	0.12

Table 1. Parameter setup of the DNS: L is domain length, n is number of grid points, Δ^+ is grid-spacing in viscous units, and Δt is the simulation time step.

Although the advective mode $(k_x - s_x, k_y - s_y)$ is one component of $\hat{M}$ (McKeon 2017; Lozano-Durán, Bae & Encinar 2020; Bae, Lozano-Duran & McKeon 2021; de Salis Young *et al.* 2024), this paper focuses on the source mode (s_x, s_y) and recipient mode (k_x, k_y).

As mentioned before, we consider modes composed with non-negative wavenumbers. The full expressions for $\hat{M}_{(s_x,s_y)(k_x,k_y)}$ with $s_x, s_y, k_x, k_y \geq 0$ are discussed in detail in Appendix A. Most result discussions in this paper centre on the mode-to-mode nonlinear energy transfer $\hat{M}$ in (2.6). For ease of reading, we sometimes omit the word 'nonlinear'. Apart from production and dissipation, energy transfer, gaining energy and losing energy in the following discussions refer to $\hat{M}$ in (2.6) due to nonlinear interactions.

Furthermore, $\hat{M}$, which represents wall-normal integrated energy transfer, satisfies the identities

$$\hat{M}_{(s_x,s_y)(k_x,k_y)} = -\hat{M}_{(k_x,k_y)(s_x,s_y)}, \tag{2.7}$$

$$\hat{M}_{(k_x,k_y)(k_x,k_y)} = 0. \tag{2.8}$$

Equation (2.7) states that the nonlinear energy transfer from mode (s_x, s_y) to mode (k_x, k_y) is equal and opposite to the nonlinear energy transfer from mode (k_x, k_y) to mode (s_x, s_y). Equation (2.8) states that each mode transfers zero energy nonlinearly to itself. Equations (2.7) and (2.8) arise from the continuity equation and the boundary conditions at the walls (the proof is in Appendix B).

Here, $\hat{P}$, $\hat{D}$, $\hat{N}$ and $\hat{M}$ represent densities of energy transfer per unit time and per unit volume.

3. Simulation parameters

The DNS are performed using a staggered-grid fourth-order finite-difference solver (Chung, Monty & Ooi 2014). Table 1 summarises the simulation parameters. For $L_x = 2\pi$ and $L_y = \pi$, the maximum wavenumbers resolved by the simulation are $k_x = \pm 55$, $k_y = \pm 110$ for $Re_\tau = 180$, and $k_x = \pm 191$, $k_y = \pm 382$ for $Re_\tau = 590$; the minimum wavenumbers are $k_x = \pm 1$, $k_y = \pm 2$ for both Reynolds numbers. The grids are evenly distributed in the streamwise and spanwise directions. In the wall-normal direction, the grid follows a Chebyshev distribution. The grid coordinate in the z direction is $z = \cos(n/N\pi)$, $z \in [-1, 1]$, where n is an integer from 0 to n_z (in table 1), and n_z is the total number of grid point in the z direction.

For $Re_\tau = 180$, the total simulation time is $20h/u_\tau$ with time step $0.002h/u_\tau$; for $Re_\tau = 590$, the total simulation time is $10h/u_\tau$ with time step $0.0002h/u_\tau$. Here, h/u_τ is used as the time unit for non-dimensionalisation. The time-averaged first- and second-order statistics of the present DNS data show good agreement with Moser, Kim & Mansour (1999), as shown in figure 1.

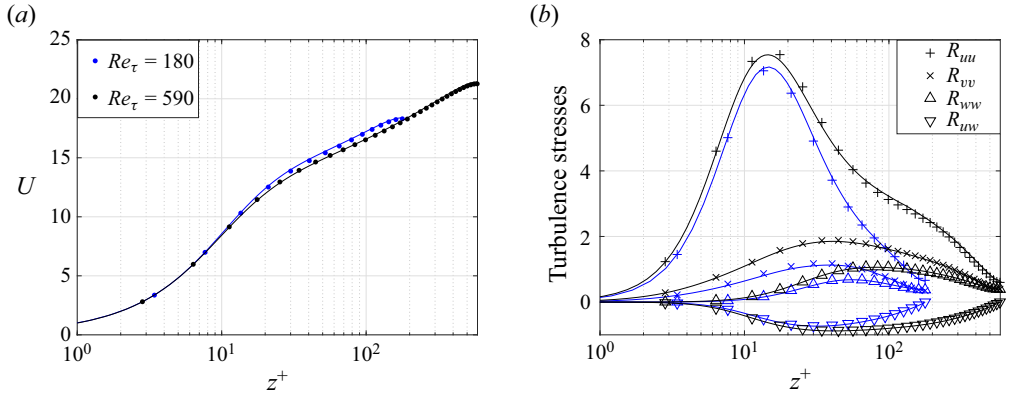

Figure 1. Comparison between the DNS dataset represented by solid lines and the standard DNS dataset (Moser *et al.* 1999) represented by discrete markers: (*a*) mean streamwise velocity; (*b*) turbulence stresses. Here, blue indicates $Re_\tau = 180$, and black indicates $Re_\tau = 590$.

4. Results

4.1. *Energy transfer distributions*

This subsection revisits the wall-normal integrated energy transfer for a single mode, as stated in (2.3*a*) (Symon *et al.* 2021). Different from Symon *et al.* (2021), we use two full channel datasets, and visualise the premultiplied energy transfer spectra, as shown in figure 2. The relationship between wavenumber and wavelength is $\lambda = 2\pi/k$, where λ refers to wavelength, and k refers to wavenumber. We see that the wall-normal integrated production spectra $\hat{P}$ (figures 2*a*,*d*) show relatively Re_τ-independent features at these two Reynolds numbers: their peaks are nearly aligned. For the wall-normal integrated dissipation spectra $\hat{D}$ (figures 2*b*,*e*), we see that there is a small peak shift towards a smaller streamwise wavelength from $Re_\tau = 180$ to $Re_\tau = 590$. The locations of the peaks are in line with the previous study that the production peak occurs at $\lambda_x^+ \approx 600$, $\lambda_y^+ \approx 100$ (at $z^+ \approx 15$), and the peak for dissipation caused by streamwise velocities occurs at $\lambda_x^+ \approx 200$, $\lambda_y^+ \approx 70$ (at $z^+ \approx 70$) (Lee & Moser 2019). The energy transfer spectra integrated along the wall-normal height at $Re_\tau = 180$ and 590 do not show significant differences, primarily because of the short outer layers at low Re_τ. The contribution from the large scales in the outer layer would become more significant as Re_τ increases (Hutchins & Marusic 2007; Lee & Moser 2019). The Reynolds–Orr equation states that the energy source for turbulence is production, and the energy sink is dissipation (Schmid & Henningson 2001). However, the energy source and sink are characterised by different structures, as large scales are responsible mainly for production and small scales are responsible mainly for dissipation. When viewed in terms of individual Fourier modes, (2.3*a*) states that the gap between production and dissipation is bridged by nonlinear energy transfer that is conservative, as shown in (2.4). As for the nonlinear energy transfer spectra $\hat{N}$ (figures 2*c*,*f*), we see the same streamwise forward cascade in which energy is transferred from large streamwise scales to small streamwise scales at $Re_\tau = 180$ and 590.

Recall that $\hat{N}$ represents the net energy that one mode receives from all other modes through nonlinear interactions. Observing figures 2(*c*,*f*), we see that there is a band of modes near $\lambda_x^+ \approx 300$ with near-zero net energy transfer $\hat{N}(k_x, k_y) \approx 0$. However, $\hat{N} = 0$ alone cannot distinguish these two possible cases: first, these modes do not participate in

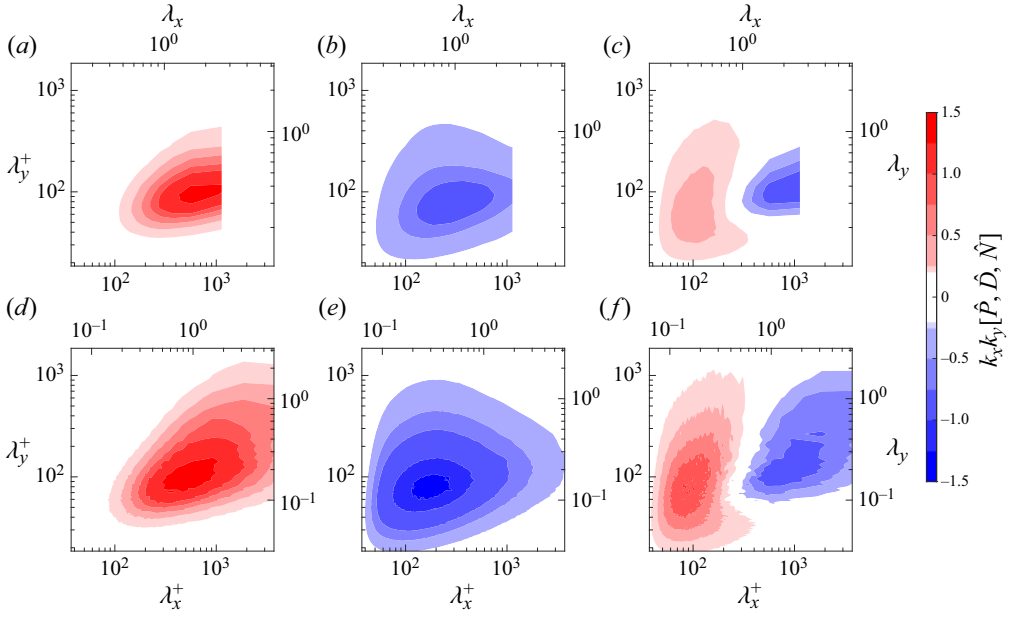

Figure 2. (*a*,*d*) Premultiplied production spectra $k_x k_y \hat{P}$. (*b*,*e*) Premultiplied (negative) dissipation spectra $k_x k_y \hat{D}$. (*c*,*f*) Premultiplied nonlinear energy transfer spectra $k_x k_y \hat{N}$. Here, (*a*,*b*,*c*) $Re_\tau = 180$ and (*d*,*e*,*f*) $Re_\tau = 590$.

nonlinear interactions; second, these modes gain and lose approximately the same amount of energy, resulting in a near-zero energy transfer. Similarly, for modes for which $\hat{N} \neq 0$, $\hat{N}$ provides only the net energy transfer for one mode without giving the detailed budget. We see the same streamwise forward cascade at $Re_\tau = 180$ and 590 (figures 2*c*,*f*) by examining $\hat{N}$. However, it is not the only piece of information that we can obtain from the nonlinear interactions. In order to explore nonlinear interactions in more detail, we investigate the mode-to-mode nonlinear energy transfer using the variable $\hat{M}_{(s_x,s_y)(k_x,k_y)}$ defined in (2.6).

4.2. *Energy transfer pathways*

We first use two examples to interpret the introduced four-dimensional variable $\hat{M}_{(s_x,s_y)(k_x,k_y)}$ that represents energy transferred nonlinearly from mode (s_x, s_y) to mode (k_x, k_y), as shown in (2.6) and Appendix A. For each example, we first choose a streamwise wavenumber and a spanwise wavenumber for mode (k_x, k_y), which remains fixed. Then we vary the streamwise and spanwise wavenumbers for mode (s_x, s_y). Both examples use the $Re_\tau = 180$ dataset. First, $\hat{M}$ is visualised with linear axes because modes containing zero wavenumbers cannot be shown on a premultiplied energy spectrum. Second, the premultiplied spectrum $s_x s_y \hat{M}$ is shown.

For the first example, we choose to fix mode (0, 6) corresponding to ($\lambda_x^+ = \infty$, $\lambda_y^+ = 188$). This mode has significant production at $Re_\tau = 180$, which means that this mode gains significant energy from the mean flow. We would like to understand how this streamwise-constant mode redistributes energy to other modes. Figure 3(*a*) shows $\hat{M}_{(s_x,s_y)(0,6)}$, which quantifies the energy that mode (0, 6) marked by the black cross

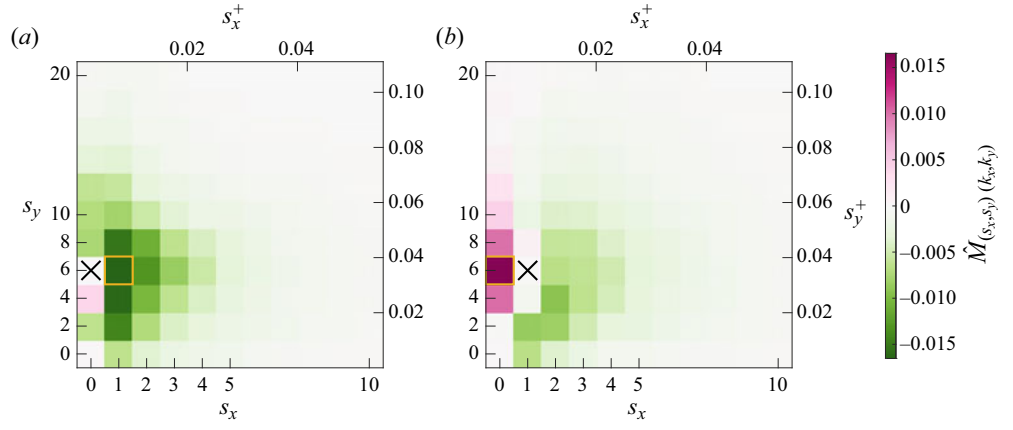

Figure 3. Plots of (*a*) $\hat{M}_{(s_x,s_y)(0,6)}$, where the black cross marks the fixed mode $(0, 6)$, and (*b*) $\hat{M}_{(s_x,s_y)(1,6)}$, where the black cross marks the fixed mode $(1, 6)$. Modes marked in orange boxes are used to illustrate the property stated in (2.7). The data are calculated for the $Re_\tau = 180$ case.

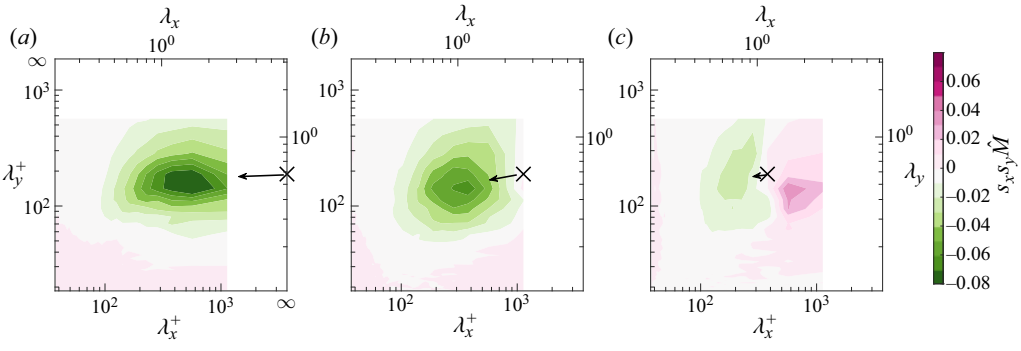

Figure 4. (*a*) The premultiplied spectrum $s_x s_y \hat{M}_{(s_x,s_y)(0,6)}$, where the black cross marks the fixed mode $(0, 6)$ corresponding to $(\lambda_x^+, \lambda_y^+) = (\infty, 188)$. (*b*) The premultiplied spectrum $s_x s_y \hat{M}_{(s_x,s_y)(1,6)}$, where the black cross marks the fixed mode $(1, 6)$ corresponding to $(\lambda_x^+, \lambda_y^+) = (1130, 188)$. (*c*) The premultiplied spectrum $s_x s_y \hat{M}_{(s_x,s_y)(3,6)}$, where the black cross marks the fixed mode $(3, 6)$ corresponding to $(\lambda_x^+, \lambda_y^+) = (377, 188)$. The arrow in each plot marks the dominant energy transfer direction.

gains from modes in pink and loses to modes in green. We see that apart from gaining energy from the wider mode $(0, 4)$ (wider in the spanwise direction), it loses energy to all other modes, including the even wider mode $(0, 2)$. The colour intensity tells us that local nonlinear energy transfer between mode $(0, 6)$ and its neighbouring modes in Fourier space is strong (Brasseur & Wei 1994; Domaradzki *et al.* 1994; Cho *et al.* 2018). In particular, mode $(0, 6)$ loses the most energy to the next smallest streamwise scales with $s_x = 1$ outlined in orange, representing a forward energy cascade. This forward cascade can also be observed from the arrow in the premultiplied spectrum in figure 4(*a*). The direction of the arrow is determined by identifying which mode receives the most energy from mode $(0, 6)$. In this case, mode $(0, 6)$ loses the most energy to mode $(1, 6)$, so the arrow points from mode $(0, 6)$ to mode $(1, 6)$. The length of the arrow is proportional to the magnitude of the energy transfer from mode $(0, 6)$ to mode $(1, 6)$.

For the second example, we choose to fix mode $(1, 6)$ corresponding to $(\lambda_x^+ = 1130, \lambda_y^+ = 188)$. Figure 3(*b*) shows $\hat{M}_{(s_x,s_y)(1,6)}$. From the first example, we see that mode $(0, 6)$ loses the most energy to this mode $(1, 6)$. The two modes highlighted in orange boxes in figures 3(*a*,*b*) have the same magnitude but opposite signs, respecting (2.7). We see the similar forward energy cascade in which mode $(1, 6)$ gains energy from the next largest streamwise scale with $s_x = 0$ and loses energy to the next smallest streamwise scale with $s_x = 2$ but larger spanwise scale with $s_y = 4$. In general, inspecting the spanwise wavenumbers, we observe that mode $(1, 6)$ loses a significant amount of energy to scales with larger spanwise wavelengths ($s_y < 6$). This corresponds to a spanwise inverse energy cascade in which energy is transferred from small spanwise scales to large spanwise scales (Cimarelli *et al.* 2013, 2016; Cho *et al.* 2018), though this inverse spanwise energy cascade is not obvious from the arrow in the premultiplied spectrum in figure 4(*b*).

Since the two selected modes $(0, 6)$ and $(1, 6)$ exhibit minimal energy gain, we further examine mode $(3, 6)$, which has a smaller streamwise wavelength. Figure 4(*c*) displays the premultiplied spectrum for mode $(3, 6)$. The results indicate that mode $(3, 6)$ gains energy from larger streamwise scales in the pink-coloured region and loses energy to smaller streamwise scales in the green-coloured region, demonstrating a streamwise forward cascade. It is worth noting that mode $(3, 6)$ loses energy to a wide range of smaller streamwise scales. The arrow indicates only the direction in which mode $(3, 6)$ loses the most energy.

For each example, we obtain one dominant energy transfer pathway from the fixed mode (k_x, k_y) to the mode to which the fixed mode (k_x, k_y) loses the most energy (as shown by the arrows in figure 4). We further sweep through a sufficient number of resolved modes as source modes, and identify their largest recipient modes. For each case, we plot an arrow pointing from the source mode to its corresponding largest recipient mode, with the length of the arrow proportional to the magnitude of the energy transfer. The path of the nonlinear energy transfer in streamwise–spanwise wavenumber space is shown in figure 5. For both $Re_\tau = 180$ and 590, we see that there are large left-pointing arrows corresponding to the forward streamwise energy cascade, and large bottom-pointing arrows corresponding to the forward spanwise energy cascade. It should be noted that each arrow in figure 5 illustrates only the dominant energy transfer pathway for each fixed (k_x, k_y) case, without showing other less dominant energy transfer pathways. In addition, the energy transfer pathways describe only the statistical properties because the variable $\hat{M}$ is a time-averaged quantity (2.6).

The two examples (figure 3) illustrate the quantification of mode-to-mode nonlinear energy transfer in streamwise–spanwise wavenumber space. For mode $(0, 6)$, we can further calculate how much energy mode $(0, 6)$ gains in total due to nonlinear interactions by summing all the modes in pink in figure 3(*a*). Similarly, we can calculate how much energy mode $(0, 6)$ loses in total due to nonlinear interactions by summing all the modes in green in figure 3(*a*). The next subsection aims to calculate the net energy transfer gain and loss due to nonlinear interactions for each mode in streamwise–spanwise wavenumber space.

4.3. *Decomposition of net nonlinear energy transfer* $\hat{N}$

With the introduced variable $\hat{M}$ in (2.5), we can decompose $\hat{N}$ for a given mode (k_x, k_y) into positive and negative contributions:

$$\hat{N}^+(k_x, k_y) = \int_0^\infty \int_0^\infty \hat{M}_{(s_x,s_y)(k_x,k_y)}\{\hat{M} > 0\}\, \mathrm{d}s_x\, \mathrm{d}s_y, \tag{4.1a}$$

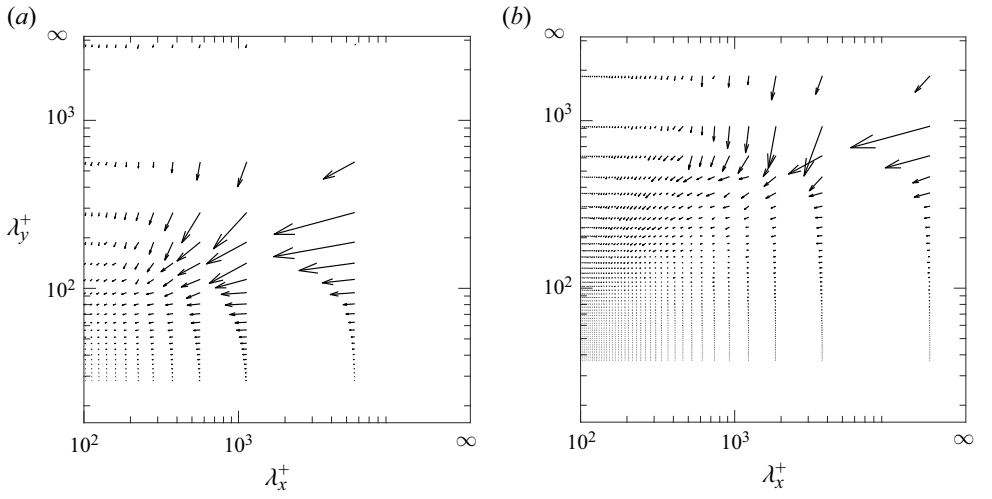

Figure 5. Dominant energy transfer pathways: (*a*) $Re_\tau = 180$, (*b*) $Re_\tau = 590$.

$$\hat{N}^-(k_x, k_y) = \int_0^\infty \int_0^\infty \hat{M}_{(s_x,s_y)(k_x,k_y)}\{\hat{M} < 0\}\,\mathrm{d}s_x\,\mathrm{d}s_y, \tag{4.1b}$$

where $\{\}$ is an indicator. An indicator is equal to 1 when the argument is true, and 0 when the argument is false. The positive energy transfer $\hat{N}^+$ quantifies the total energy that mode (k_x, k_y) gains from other modes. The negative energy transfer $\hat{N}^-$ quantifies the total energy that mode (k_x, k_y) loses to other modes. According to (2.5), these two variables are linked to the net energy transfer $\hat{N}$ by

$$\hat{N}(k_x, k_y) = \hat{N}^+(k_x, k_y) + \hat{N}^-(k_x, k_y). \tag{4.2}$$

The triadic interaction in the streamwise–spanwise wavenumber space enables this decomposition. However, it is important to note that $\hat{N}^+$ and $\hat{N}^-$ do not provide a complete picture of energy gain and loss, as $\hat{M}$ is derived through wall-normal integration and time averaging.

Figure 6(*a*,*b*) quantify the energy transfer gain and loss for each mode at $Re_\tau = 180$. We see the dual characteristic of nonlinear energy transfer that each mode acts as an energy source and energy recipient. The difference between the energy transfer gain and loss for each mode results in the net nonlinear energy transfer spectrum $\hat{N}$, as shown in figure 6(*c*) and respecting equation (4.2). Figure 6(*c*) is the same as figure 2(*c*) and figure 6(*f*) is the same as figure 2(*f*). We see that the mode marked by the black cross where $\hat{N} \approx 0$ in figure 6(*c*) has non-negligible net energy loss and net energy gain as observed in the corresponding locations in figure 6(*a*,*b*). This indicates that this mode gains and loses approximately equal amount of energy, resulting in near-zero net nonlinear energy transfer. The production and dissipation spectra show that large scales lose energy because they gain the most energy through production, while small scales gain energy to dissipate it. This results in intermediate scales with a net zero $\hat{N}$. The $\hat{N}^+$ and $\hat{N}^-$ spectra indicate that energy gain and loss transition 'smoothly' across scales for the Reynolds numbers considered. However, this is not necessarily true for high-Reynolds-number flows.

Now we answer the other question raised at the end of § 4.1. As mentioned previously, the net energy transfer spectra $\hat{N}$ reveal the same streamwise forward cascade at $Re_\tau = 180$

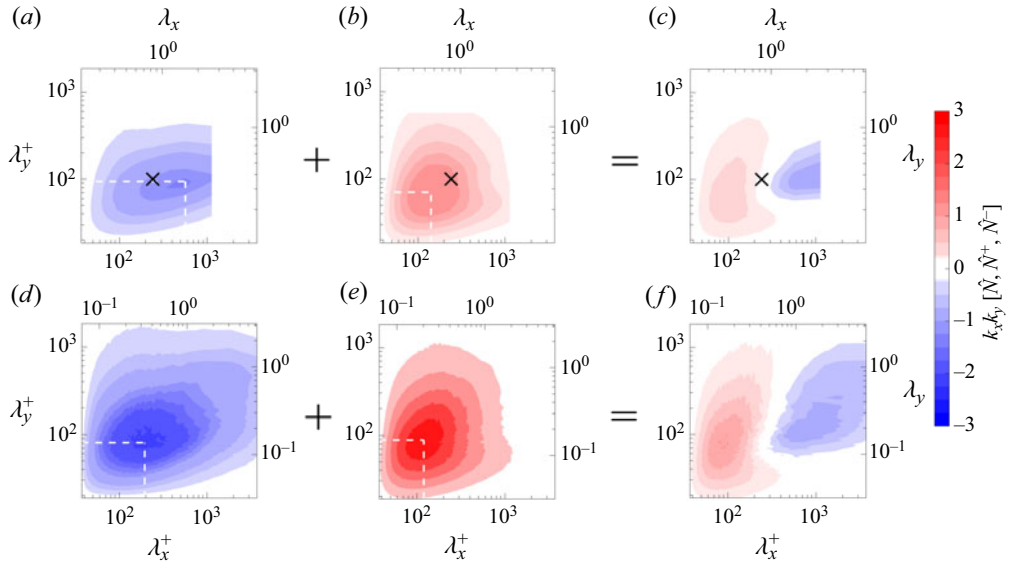

Figure 6. Decomposition of the net nonlinear energy transfer: $\hat{N}^- + \hat{N}^+ = \hat{N}$. (*a*,*d*) Premultiplied negative nonlinear energy transfer spectra $k_x k_y \hat{N}^-$, where dashed lines mark the peak. (*b*,*e*) Premultiplied positive nonlinear energy transfer spectra $k_x k_y \hat{N}^+$, where dashed lines mark the peak, (*c*,*f*) Premultiplied net nonlinear energy transfer spectra $k_x k_y \hat{N}$. Here, (*a*–*c*) $Re_\tau = 180$, and (*d*–*f*) $Re_\tau = 590$. The black crosses in (*a*–*c*) mark a mode with $\hat{N} \approx 0$ for explanation purposes.

and 590 (figures 6*c*,*f*). At $Re_\tau = 180$, we see that the negative energy transfer spectrum $\hat{N}^-$ peak is at $\lambda_x^+ \approx 600$, $\lambda_y^+ \approx 100$, and the positive energy transfer spectrum $\hat{N}^+$ peak is at $\lambda_x^+ \approx 150$, $\lambda_y^+ \approx 70$, indicated by the white dashed lines in figures 6(*a*,*b*). This indicates that large streamwise scales lose the most energy, and small streamwise scales gain the most energy. Thus figures 6(*a*,*b*) illustrate the streamwise forward cascade, which aligns with the net energy transfer spectrum (figure 6*c*).

At $Re_\tau = 590$, we see that the negative energy transfer spectrum $\hat{N}^-$ peak is at $\lambda_x^+ \approx 200$, $\lambda_y^+ \approx 90$, and the positive energy transfer spectrum $\hat{N}^+$ peak is at $\lambda_x^+ \approx 150$, $\lambda_y^+ \approx 80$, indicated by the white dashed lines in figures 6(*d*,*e*). From $Re_\tau = 180$ to 590, there is a significant negative energy transfer spectrum peak shift to a much smaller λ_x^+. The spectra of $\hat{N}^+$ and $\hat{N}^-$ reveal the same streamwise forward cascade as $\hat{N}$, because of (4.2). The shift of $\hat{N}^-$ peak cannot be deduced directly from the production and dissipation spectra, because $\hat{N}^-$ is obtained through the triadic interaction. The reason for this shift remains unclear at this stage. Note that the above discussions are for the whole channel since $\hat{M}$ is wall-normal integrated nonlinear energy transfer that hides the nonlinear energy transfer in the wall-normal direction.

4.4. *Nonlinear energy transfer of three specific modes*

Linear analysis explains the energy amplification mechanisms of different modes (Schmid & Henningson 2001; Jovanović & Bamieh 2005), leaving the nonlinear part relatively unexplored. Since nonlinear energy transfer is conservative, the nonlinear energy transfer among different modes should be interpreted as energy redistribution. In this

subsection, we use $\hat{M}$ to investigate the energy redistribution of three different modes: streamwise-constant modes, oblique 2 : 1 modes and spanwise-constant modes.

Following Jovanović & Bamieh (2005), we define the nonlinear energy transfer of the streamwise-constant modes as

$$\hat{M}_{(s_x,s_y)(k_x=0)} = \sum_{k_x=0} \hat{M}_{(s_x,s_y)(k_x,k_y)}. \tag{4.3}$$

Oblique waves are characterised by $k_x \approx O(1)$, $k_y \approx O(1)$. Considering the geometry of the channel box used in this study, we define the nonlinear energy transfer of the oblique 2 : 1 modes (where 2 : 1 refers to $L_x/L_y = 2:1$) as

$$\hat{M}_{(s_x,s_y)(k_y=2k_x)} = \sum_{k_y=2k_x} \hat{M}_{(s_x,s_y)(k_x,k_y)}. \tag{4.4}$$

We define the nonlinear energy transfer of the spanwise-constant modes as

$$\hat{M}_{(s_x,s_y)(k_y=0)} = \sum_{k_y=0} \hat{M}_{(s_x,s_y)(k_x,k_y)}. \tag{4.5}$$

Figure 7 shows the nonlinear energy transfer of the three different modes at $Re_\tau = 180$ and 590. As for the interpretation of each subplot, the specific modes (indicated by the black crosses) gain energy from modes in pink, and lose energy to modes in green. We see that the streamwise-constant modes (figures 7*a*,*d*) lose energy to smaller streamwise scales ($s_x > 0$), exhibiting a streamwise forward cascade. This could be linked to streak breakdown which is one phase of the self-sustaining process. Due to the instability of long streamwise streaks, they break down into smaller streamwise streaks (Hamilton *et al.* 1995). The breakdown of streamwise streaks has been observed both experimentally (Blackwelder & Eckelmann 1979) and numerically (Hwang & Bengana 2016). For the oblique 2 : 1 modes (figures 7*b*,*e*), we see that they generally gain energy from scales with larger aspect ratios s_y/s_x (which is equivalent to k_y/k_x) (Symon *et al.* 2021), and lose energy to scales with smaller aspect ratios, exhibiting a transverse cascade (Lee & Moser 2019; Symon *et al.* 2021). For the spanwise-constant modes (figures 7*c*,*f*), we see that they mainly gain energy from smaller spanwise scales, exhibiting a spanwise inverse cascade (Cimarelli *et al.* 2013, 2016; Cho *et al.* 2018). If we think of the streamwise-constant modes with infinite aspect ratio $s_y/s_x \to \infty$ and the spanwise-constant modes with zero aspect ratio $s_y/s_x \to 0$, then we could conclude that there exists energy transfer from scales with large aspect ratio to scales with small aspect ratio. In terms of the shapes of scales, this transverse cascade refers to energy transfer from streamwise-elongated scales to spanwise-elongated scales. It is also worth noting that the transverse cascade of the three modes is not substantially influenced by the Reynolds number for this range.

The above discussion tells us that the transverse energy cascade is related to s_y/s_x (which is equivalent to k_y/k_x). We can also visualise this same piece of information on a log-polar coordinate in which s_y/s_x corresponds to a certain slope (Lee & Moser 2019), as shown in figure 8. Following Lee & Moser (2019), $s_x^\# = \xi s_x/\sqrt{s_x^2+s_y^2}$, $s_y^\# = \xi s_y/\sqrt{s_x^2+s_y^2}$ and $\xi = \log(\sqrt{s_x^2+s_y^2}/k_{ref})$, with $k_{ref} = Re_\tau/50\,000$. From figures 8(*a*,*d*), the streamwise-constant modes located on the $s_x^\# = 0$ axis lose energy to other modes, corresponding to the finding that modes located on the $s_x^\# = 0$ axis have significant net negative nonlinear energy transfer (Lee & Moser 2019). From figures 8(*b*,*e*), the oblique

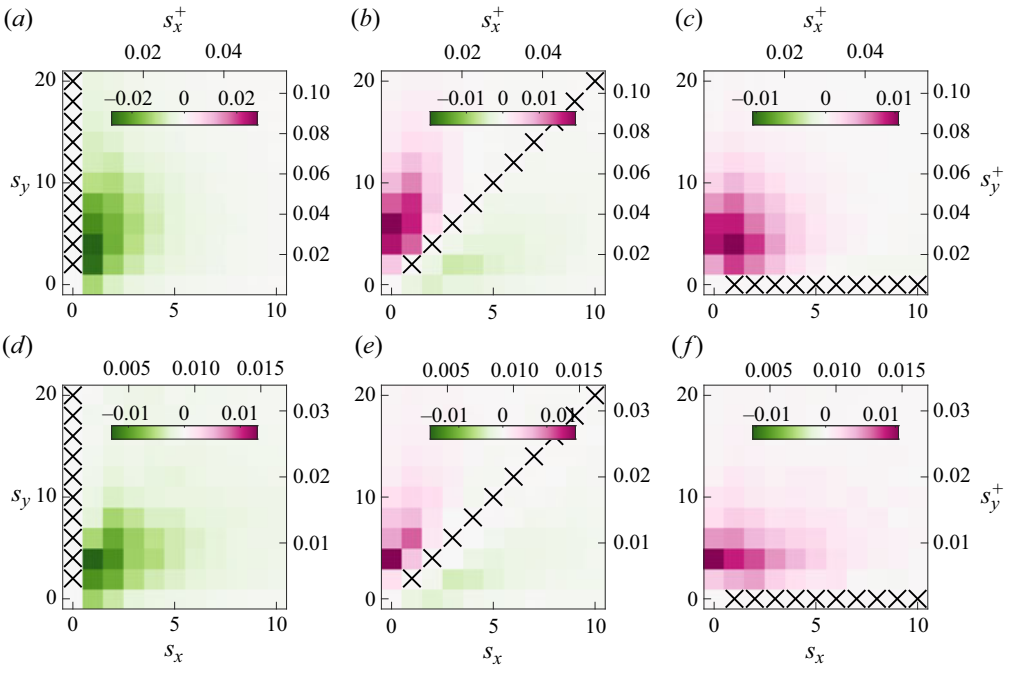

Figure 7. Plots of (a,d) $\hat{M}_{(s_x,s_y)(k_x=0)}$, (b,e) $\hat{M}_{(s_x,s_y)(k_y=2k_x)}$, (c,f) $\hat{M}_{(s_x,s_y)(k_y=0)}$, visualised using discrete modes. Here, $(a–c)$ $Re_\tau = 180$, and $(d–f)$ $Re_\tau = 590$. Black crosses mark the modes of the investigated structures.

2 : 1 modes located on $s_y^\# = 2s_x^\#$ gain energy from modes satisfying $s_y^\# > 2s_x^\#$, and lose energy to modes satisfying $s_y^\# < 2s_x^\#$, corresponding to the transverse cascade mentioned previously. From figures 8(c,f), the spanwise-constant modes located on the $s_y^\# = 0$ axis mainly gain energy but also lose a small amount of energy. We see that one advantage of using log-polar premultiplied spectra over the traditional premultiplied spectra is that we can visualise modes that contain one zero wavenumber (either $s_x = 0$ or $s_y = 0$).

Note that the above discussion concerns only the nonlinear energy transfer as one component in the energy transfer balance (2.3a). One should not interpret this as saying that energy merely originates from the streamwise-constant modes, goes through the oblique 2 : 1 modes, and finally dissipates at the spanwise-constant modes. Equation (2.3a) gives the energy transfer budget for each mode. To evaluate the overall energy transfer balance comprehensively, we need to consider the production and dissipation as well. Motivated by § 4.3, we decompose the net nonlinear energy transfer of each mode into its positive and negative parts. According to (2.3a) and (4.2), for each mode, the energy transfer budget is

$$\hat{P} + \hat{D} + \hat{N}^+ + \hat{N}^- = 0. \tag{4.6}$$

The energy budgets (2.3a) for the three modes are shown in figure 9. For the streamwise-constant modes, they receive a large amount of energy from the mean flow through production, as seen from the blue bars, and they lose a large amount of energy nonlinearly to other modes, as seen from the purple bars. For the oblique 2 : 1 modes, apart from gaining energy from the mean flow and dissipating energy, they gain and lose energy

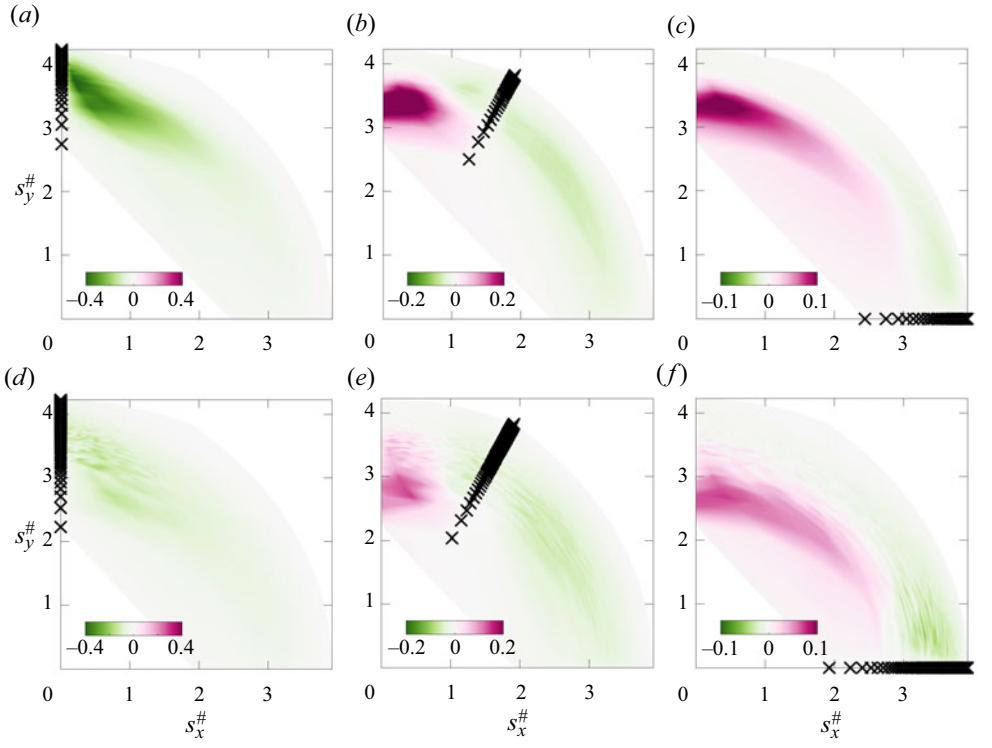

Figure 8. Log-polar premultiplied energy spectra (*a*,*d*) $((s_x^2+s_y^2)/\xi)\,\hat{M}_{(s_x,s_y)(k_x=0)}$, (*b*,*e*) $((s_x^2+s_y^2)/\xi)\,\hat{M}_{(s_x,s_y)(k_y=2k_x)}$, (*c*,*f*) $((s_x^2+s_y^2)/\xi)\,\hat{M}_{(s_x,s_y)(k_y=0)}$. Here, (*a*–*c*) $Re_\tau = 180$, and (*d*–*f*) $Re_\tau = 590$. Black crosses mark the modes of the investigated structures.

nonlinearly through interacting with other modes, as seen from the purple and yellow bars. For the spanwise-constant modes, the only energy gain is through nonlinear energy transfer, as seen from the yellow bars. The streamwise-constant modes and the oblique 2 : 1 modes gain energy from the mean flow (positive production), while the spanwise-constant modes lose energy to the mean flow (negative production). Dissipation occurs for all three modes as seen from the red bars. Although the values are different at the two Reynolds numbers, different types of energy transfer show similar trends in the three modes.

Having discussed the three types of modes, we proceed to discuss a certain type of structure. It has been found that streamwise-constant modes with spanwise wavelengths $\lambda_y^+ \approx 100$ experience significant energy growth due to linear mechanisms (Pujals *et al.* 2009; Hwang & Cossu 2010). Using the variable $\hat{M}$, we can investigate the nonlinear energy transfer of this specific structure. We define the mode-to-mode nonlinear energy transfer of streamwise streaks with $\lambda_y^+ \approx 100$ as

$$\hat{M}_{(s_x,s_y)(streaks)} = \sum_{k_x=0,\lambda_y^+\approx 100} \hat{M}_{(s_x,s_y)(k_x,k_y)}. \tag{4.7}$$

Figure 10 shows the log-polar premultiplied energy spectra of streamwise streaks at $Re_\tau = 180$ and 590. According to the definition in (4.7), the discussed streamwise streaks have zero streamwise wavenumber $k_x = 0$, corresponding to $s_x^\# = 0$. The discussed streamwise streaks have spanwise wavelength $\lambda_y^+ \approx 100$, corresponding to $s_y^\# = 3.49$.

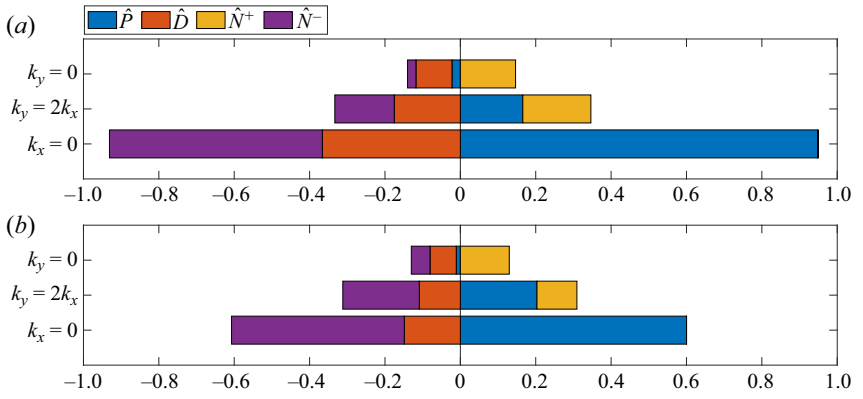

Figure 9. Energy budgets for the streamwise-constant mode ($k_x = 0$), oblique 2 : 1 mode ($k_y = 2k_x$) and spanwise-constant mode ($k_y = 0$). Here, (*a*) $Re_\tau = 180$, and (*b*) $Re_\tau = 590$.

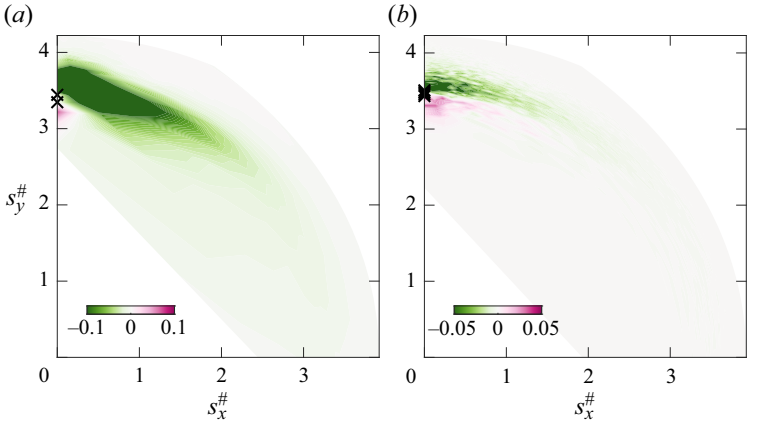

Figure 10. Log-polar premultiplied energy spectra of streamwise streaks $((s_x^2 + s_y^2)/\xi)\,\hat{M}_{(s_x,s_y)(streaks)}$. Black crosses mark the modes satisfying $k_x = 0$ and $\lambda_y^+ \approx 100$. Here, (*a*) $Re_\tau = 180$, and (*b*) $Re_\tau = 590$.

We see that the streamwise streaks mainly lose energy to smaller scales at $Re_\tau = 180$ and 590. The main difference from figures 8(*a*,*d*) is that the streamwise streaks receive a small amount of energy from large scales, as indicated by the pink colour.

4.5. *Forward cascade and inverse cascade*

In this subsection, we use $\hat{M}$ to quantify the forward and inverse cascades between the large scales and small scales in the spirit of LES. For channel flows, resolved scales could be set by modes belonging to a rectangular region determined by the conditions $k_x \leq k_{xC}$ and $k_y \leq k_{yC}$, where k_{xC} and k_{yC} are cutoff wavenumbers (Germano *et al.* 1991; Domaradzki *et al.* 1994; Härtel *et al.* 1994). These cutoff wavenumbers are determined by the choice of a single variable n_C:

$$k_{xC} = \frac{2\pi n_C}{L_x}, \quad k_{yC} = \frac{2\pi n_C}{L_y}. \tag{4.8a,b}$$

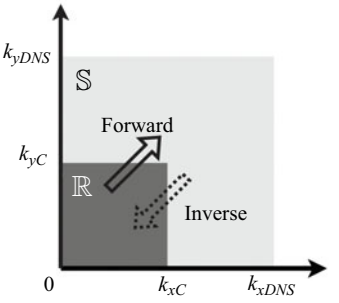

Figure 11. A sketch illustrating the forward cascade and inverse cascade between the resolved-scale region $\mathbb{R}$ marked in dark grey and the subgrid-scale region $\mathbb{S}$ marked in light grey. Region $\mathbb{R}$ contains the resolved scales, and region $\mathbb{S}$ contains the subgrid scales. Here, k_{xC} and k_{yC} are the cutoff wavenumbers, and k_{xDNS} and k_{yDNS} are the maximum wavenumbers resolved by DNS.

One issue of subgrid-scale energy transfer modelling with eddy viscosity is that it assumes that the subgrid scales only dissipate energy and neglects the energy transferred from the subgrid scales to the resolved scales, also known as 'backscatter' (Piomelli *et al.* 1991). Figure 11 illustrates the two-way energy transfer between the resolved scales and subgrid scales. We aim to quantify the forward cascade and inverse cascade using mode-to-mode nonlinear energy transfer $\hat{M}$.

Recall that $\hat{M}_{(s_x,s_y)(k_x,k_y)}$ represents energy transfer from mode (s_x, s_y) to mode (k_x, k_y). For the forward cascade, energy is transferred from the resolved scales in region $\mathbb{R}$ to the subgrid scales in region $\mathbb{S}$, as indicated by the solid arrow in figure 11. Similar to (4.1*a*) and (4.1*b*), for this forward cascade, we can calculate the energy lost by each mode (4.9*b*) in the resolved-scale region $\mathbb{R}$ and the energy gained by each mode (4.9*a*) in the subgrid-scale region $\mathbb{S}$:

$$\hat{N}_F^+(k_x, k_y, n_C) = \iint \hat{M}_{(s_x,s_y)(k_x,k_y)}\{\hat{M} > 0, (s_x, s_y) \in \mathbb{R}, (k_x, k_y) \in \mathbb{S}\}\,\mathrm{d}s_x\,\mathrm{d}s_y, \quad (4.9a)$$

$$\hat{N}_F^-(k_x, k_y, n_C) = \iint \hat{M}_{(s_x,s_y)(k_x,k_y)}\{\hat{M} < 0, (s_x, s_y) \in \mathbb{S}, (k_x, k_y) \in \mathbb{R}\}\,\mathrm{d}s_x\,\mathrm{d}s_y. \quad (4.9b)$$

Figure 12 shows an example of the forward cascade from the resolved scales to the subgrid scales at $Re_\tau = 180$. The choice of cutoff wavenumber $n_C = 5$ corresponds to the filtering width Δ_i satisfying $\Delta_i \approx 5\Delta x_i$ $(i = 1, 2)$ at $Re_\tau = 180$. Figure 12(*a*) shows that streamwise-elongated modes with large k_y/k_x in region $\mathbb{R}$ lose the most energy. Figure 12(*b*) shows that modes gaining energy in region $\mathbb{S}$ do not show significant preference with respect to k_y/k_x.

For the inverse cascade, energy is transferred from the subgrid scales in region $\mathbb{S}$ to the resolved scales in region $\mathbb{R}$, as indicated by the dashed-line arrow in figure 11. Similar to (4.1*a*) and (4.1*b*), for this inverse cascade, we can calculate the energy gained by each mode (4.10*a*) in the resolved-scale region $\mathbb{R}$, and the energy lost by each mode (4.10*b*) in the subgrid-scale region $\mathbb{S}$:

$$\hat{N}_I^+(k_x, k_y, n_C) = \iint \hat{M}_{(s_x,s_y)(k_x,k_y)}\{\hat{M} > 0, (s_x, s_y) \in \mathbb{S}, (k_x, k_y) \in \mathbb{R}\}\,\mathrm{d}s_x\,\mathrm{d}s_y, \quad (4.10a)$$

$$\hat{N}_I^-(k_x, k_y, n_C) = \iint \hat{M}_{(s_x,s_y)(k_x,k_y)}\{\hat{M} < 0, (s_x, s_y) \in \mathbb{R}, (k_x, k_y) \in \mathbb{S}\}\,\mathrm{d}s_x\,\mathrm{d}s_y. \quad (4.10b)$$

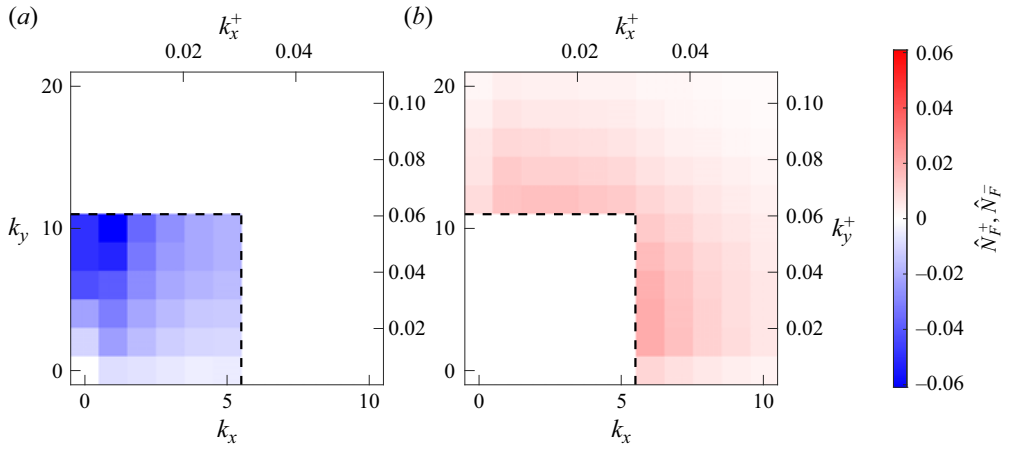

Figure 12. An example of the forward cascade, where $n_C = 5$ corresponds to ($\lambda_x^+ = 226$, $\lambda_y^+ = 113$) at $Re_\tau = 180$: (*a*) $\hat{N}_F^-(k_x, k_y, 5)$ shows the energy lost by resolved scales in region $\mathbb{R}$; (*b*) $\hat{N}_F^+(k_x, k_y, 5)$ shows the energy gained by subgrid scales in region $\mathbb{S}$. Dashed lines mark the boundary between the resolved-scale region $\mathbb{R}$ and the subgrid-scale region $\mathbb{S}$. Note that the maximum wavenumbers in this figure are not the maximum wavenumbers resolved in the DNS.

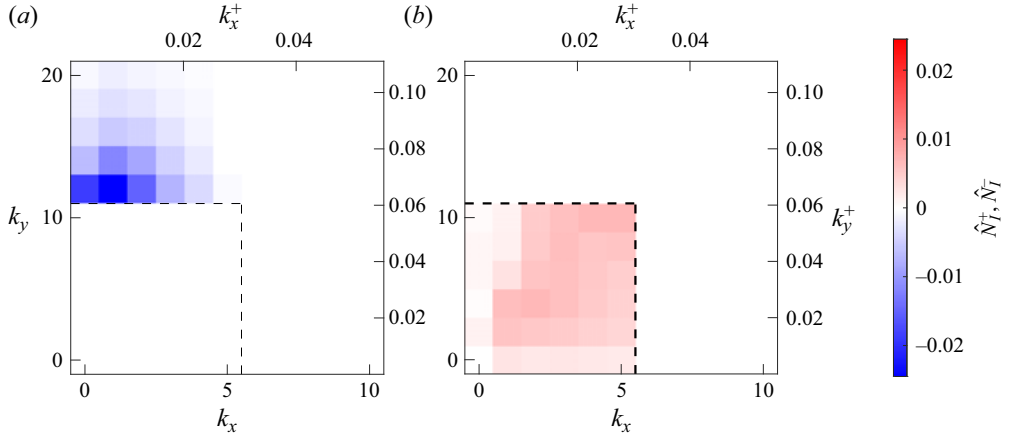

Figure 13. Inverse cascade example: $n_C = 5$ ($\lambda_x^+ = 226$, $\lambda_y^+ = 113$) at $Re_\tau = 180$. Here, (*a*) $\hat{N}_I^-(k_x, k_y, 5)$ shows how subgrid scales in region $\mathbb{S}$ lose energy; (*b*) $\hat{N}_I^+(k_x, k_y, 5)$ shows how resolved scales in region $\mathbb{R}$ gain energy.

Figure 13 shows an example of the inverse cascade from the subgrid scales to the resolved scales at $Re_\tau = 180$. Figure 13(*a*) shows the asymmetry of modes losing energy in region $\mathbb{S}$: only streamwise elongated modes with large k_y/k_x lose energy. Figure 13(*b*) shows that modes gaining energy in region $\mathbb{R}$ do not show significant preference with respect to k_y/k_x.

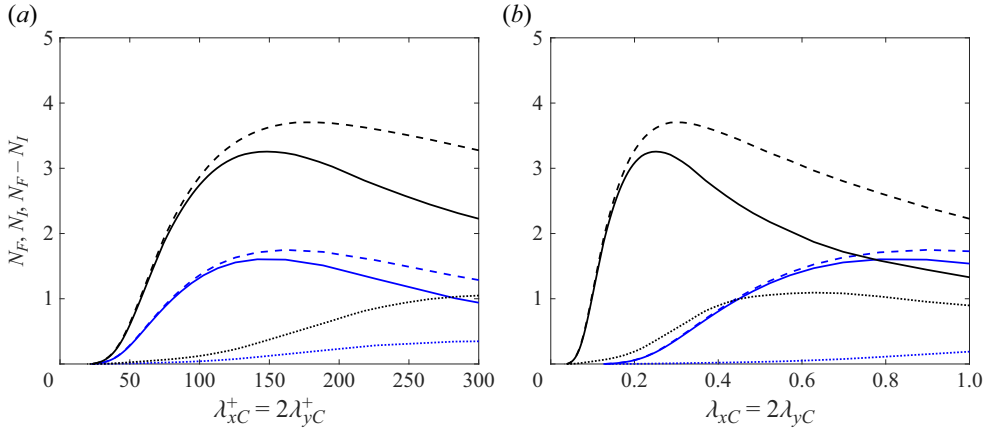

Figure 14. Quantification of the energy transfer between the resolved scales and subgrid scales: (*a*) cutoff wavelengths are scaled in inner units; (*b*) cutoff wavelengths are scaled in outer units. Dashed lines indicate forward cascade N_F; dotted lines indicate inverse cascade N_I; solid lines indicate net energy cascade $N_F - N_I$. Blue indicates $Re_\tau = 180$; black indicates $Re_\tau = 590$.

We further quantify the forward cascade and inverse cascade between the resolved scales and subgrid scales determined by n_C:

$$N_F(n_C) = \iint_{\mathbb{S}} \hat{N}_F^+ \,\mathrm{d}k_x \,\mathrm{d}k_y \overset{(2.7)}{=} -\iint_{\mathbb{R}} \hat{N}_F^- \,\mathrm{d}k_x \,\mathrm{d}k_y, \tag{4.11}$$

$$N_I(n_C) = \iint_{\mathbb{R}} \hat{N}_I^+ \,\mathrm{d}k_x \,\mathrm{d}k_y \overset{(2.7)}{=} -\iint_{\mathbb{S}} \hat{N}_I^- \,\mathrm{d}k_x \,\mathrm{d}k_y. \tag{4.12}$$

The forward cascade and inverse cascade calculated using (4.11) and (4.12) for $Re_\tau = 180$ and 590 are shown in figure 14. A general criterion for LES is to resolve a sufficient amount of large scales that should contain 80 % of the total kinetic energy (Pope 2000). By checking the DNS datasets, we know that scales with $\lambda_x^+ = 2\lambda_y^+ > 162$ need to be resolved at $Re_\tau = 180$, and scales with $\lambda_x^+ = 2\lambda_y^+ > 232$ need to be resolved at $Re_\tau = 590$. Therefore, we need to consider the energy transfer when the cutoff wavelengths satisfy $\lambda^+_{xC} = 2\lambda^+_{yC} < 162$ at $Re_\tau = 180$, and $\lambda^+_{xC} = 2\lambda^+_{yC} < 232$ at $Re_\tau = 590$. We see that the forward cascade is at least four times larger than the inverse cascade when $\lambda^+_{xC} < 250$, indicating that the net energy transfer is from the resolved scales to the subgrid scales, shown by the solid lines. This justifies why eddy viscosity considering only the forward cascade is used in LES (Pope 2000). The net forward cascade from resolved scales to subgrid scales could also be expected from figure 2. Large scales are mainly responsible for production, and small scales are mainly responsible for dissipation. The imbalance between production and dissipation in terms of each scale results in the net forward energy cascade. However, the inverse cascade is not negligible when $\lambda^+_{xC} > 100$, so the negligence of it has been proposed as a source of inaccuracy in LES (Anderson & Domaradzki 2012; Cimarelli & De Angelis 2014).

When interpreting figure 14, two things should be noted. First, the results would be different if the aspect ratio between the streamwise and spanwise cutoff wavenumbers $k_{xC}/k_{yC} = \frac{1}{2}$ were changed. Second, the above results represent only the wall-normal integrated forward and inverse cascades. Due to the inhomogeneity in the wall-normal

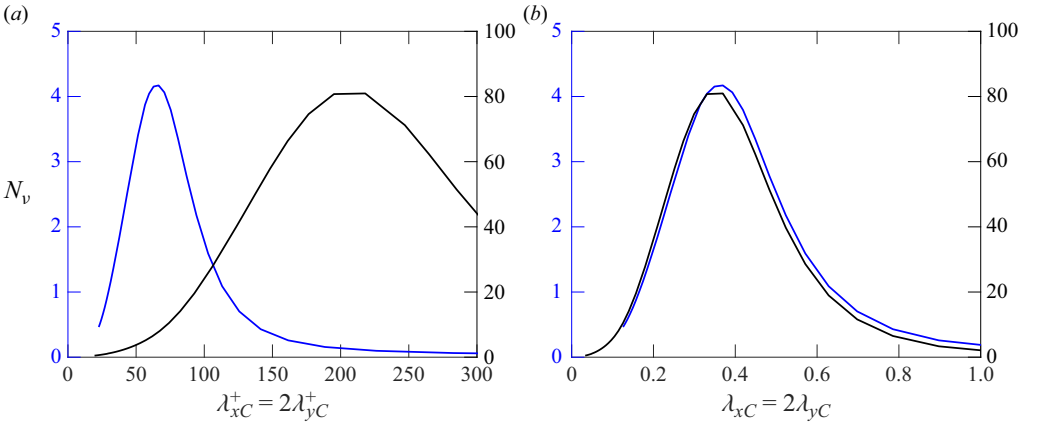

Figure 15. Forward cascade N_ν predicted by the eddy viscosity (4.14) in (*a*) inner units, (*b*) outer units. Blue indicates $Re_\tau = 180$, left-hand axis; black indicates $Re_\tau = 590$, right-hand axis.

direction of wall-bounded flows, the forward cascade and inverse cascade would vary with wall-normal height.

Now we compare the energy cascade calculated using $\hat{M}$ with the eddy viscosity method. The forward cascade from the resolved scales to the subgrid scales N_ν can be calculated using the linear eddy viscosity model (Pope 2000)

$$N_\nu = \nu \tilde{S}^2, \tag{4.13}$$

where ν is the eddy viscosity, $\tilde{S}$ is the characteristic filtered rate of strain $\tilde{S} = (2\tilde{S}_{ij}\tilde{S}_{ij})^{1/2}$, $\tilde{S}_{ij}$ is the filtered rate-of-strain tensor $\tilde{S}_{ij} = \frac{1}{2}(\partial\tilde{u}_i/\partial x_j + \partial\tilde{u}_j/\partial x_i)$, and $\tilde{u}_i$ is the filtered velocity of the resolved scales.

We can use the Smagorinsky eddy viscosity (Smagorinsky 1963)

$$\nu = (C_s D_z \Delta)^2 \tilde{S}, \tag{4.14}$$

where C_s is the Smagorinsky coefficient, set to be $C_s = 0.067$ (Moin & Kim 1982), and D_z is the damping function that accounts for low-Reynolds-number subgrid-scale stress near the wall, set to be $D_z = 1 - \exp(-z^+/25)$ (Moin & Kim 1982). Since we do not apply filtering in the wall-normal direction, the characteristic length scale of the largest subgrid-scale eddies Δ is set to be $\Delta = (\Delta_1\Delta_2)^{1/2}$. After we have obtained the filtered velocity fields $\tilde{u}_i$ using the cutoff wavenumbers (4.8*a*,*b*) in Fourier space, we calculate the forward cascade N_ν in (4.13) and the Smagorinsky eddy viscosity ν in (4.14) directly in physical space.

Figure 15 shows the forward cascades from the resolved scales to subgrid scales predicted by the eddy viscosity (4.14) at $Re_\tau = 180$ and 590. We see that the forward cascade at $Re_\tau = 590$ is approximately 20 times higher than the forward cascade at $Re_\tau = 180$. We do not put the forward cascades predicted from (4.14) and from $\hat{M}$ on the same figure because they differ in magnitude substantially. Nevertheless, both the eddy viscosity (4.14) and $\hat{M}$ are able to predict the forward cascades with respect to cutoff wavelengths with the same shape. The forward cascade predicted by the eddy viscosity (4.14) first increases as the cutoff wavelengths (λ_{xC} and λ_{yC}) decrease, and then decreases to zero as the cutoff wavelengths approach the DNS grid sizes, aligning with the trends in figure 14. The substantial mismatch in magnitude between the eddy viscosity (4.14) and

$\hat{M}$ is that $\hat{M}$ represents the wall-normal integrated energy transfer and is a time-averaged variable. Statistics of energy transfer has been averaged out in the wall-normal direction and the time domain, which could be more prominent at $Re_\tau = 590$. That is the main reason why $N_F - N_I$ in figure 14 is substantially smaller than N_v in figure 15. Nevertheless, $\hat{M}$ could be extended to include the wall-normal coordinate, and $N_F - N_I$ can be calculated at each wall-normal height before being time and wall-normal averaged.

5. Conclusions and outlook

We investigate nonlinear energy transfer in turbulent channel flow in Fourier space at $Re_\tau = 180$ and 590. We introduce a four-dimensional variable $\hat{M}_{(s_x,s_y)(k_x,k_y)}$ that describes the nonlinear energy transfer between any two modes in streamwise–spanwise wavenumber space, by analysing the individual triadic interactions of the nonlinear energy transfer term in the spectral turbulent kinetic energy equation.

We use this variable to explore three things. First, we decompose the net nonlinear energy transfer $\hat{N}$ into its positive and negative contributions: $\hat{N}^+$ and $\hat{N}^-$. This allows us to separately quantify the total energy gained and total energy lost by each mode. Second, we investigate the nonlinear energy transfer of three specific modes. We observe that there exists energy transfer from streamwise-elongated structures to spanwise-elongated structures, and that this transverse cascade is characterised by the aspect ratio k_y/k_x. Third, we quantify the forward cascade and inverse cascade between the resolved scales and subgrid scales in the spirit of LES. For both Reynolds numbers considered, the forward cascade is significantly larger than the inverse cascade when $\lambda_{xC}^+ < 250$, justifying why eddy viscosity considers only the forward cascade used in LES. However, the inverse cascade is not negligible when $\lambda_{xC}^+ > 100$. We also compare the energy cascade calculated using $\hat{M}$ with the Smagorinsky eddy viscosity. The forward cascades calculated from the two methods show a substantial deviation in magnitude and a similar trend with respect to the cutoff wavelengths.

The pathways illustrated by $\hat{M}$ represent a nonlinear energy transfer network in two-dimensional Fourier space (Gürcan, Li & Morel 2020). A promising area for future work would be to extend mode-to-mode nonlinear energy transfer $\hat{M}_{(s_x,s_y)(k_x,k_y)}$ to include another dimension, the wall-normal coordinate, to investigate the details of mode-to-mode nonlinear energy transfer at any wall-normal height.

Funding. This research was supported by the University of Melbourne's Research Computing Services and the Petascale Campus Initiative.

Declaration of interests. The authors report no conflict of interest.

Author ORCIDs.
Jitong Ding https://orcid.org/0000-0003-3646-8441;
Daniel Chung https://orcid.org/0000-0003-3732-364X;
Simon J. Illingworth https://orcid.org/0000-0002-7545-9786.

Appendix A. Full expression for $\hat{M}_{(s_x,s_y)(k_x,k_y)}$

Mode-to-mode nonlinear energy transfer $\hat{M}$ is formulated from $\hat{N}$:

$$\hat{N}(k_x, k_y) = -\left\langle \hat{u}_i^{(k_x,k_y)}, \widehat{\frac{\partial u_i u_j}{\partial x_j}}^{(k_x,k_y)} \right\rangle \overset{\text{continuity}}{=} -\left\langle \hat{u}_i^{(k_x,k_y)}, \widehat{u_j \frac{\partial u_i}{\partial x_j}}^{(k_x,k_y)} \right\rangle. \tag{A1}$$

If we assign $f_i = -u_j(\partial u_i/\partial x_j)$, then $\hat{N}$ could be expressed according to three different cases:

$$\underset{(k_x,k_y\in\mathbb{R}^+)}{\hat{N}(k_x,k_y)} = (\hat{f}_i^{(k_x,k_y)}\,\hat{u}_i^{(-k_x,-k_y)} + \hat{f}_i^{(-k_x,k_y)}\,\hat{u}_i^{(k_x,-k_y)} + \text{c.c.})$$
$$= 2\,\text{Real}\{\hat{f}_i^{(k_x,k_y)}\,\hat{u}_i^{(-k_x,-k_y)} + \hat{f}_i^{(-k_x,k_y)}\,\hat{u}_i^{(k_x,-k_y)}\}, \tag{A2a}$$
$$\underset{(k_y\in\mathbb{R}^+)}{\hat{N}(0,k_y)} = (\hat{f}_i^{(0,k_y)}\,\hat{u}_i^{(0,-k_y)} + \text{c.c.}) = 2\,\text{Real}\{\hat{f}_i^{(0,k_y)}\,\hat{u}_i^{(0,-k_y)}\}, \tag{A2b}$$
$$\underset{(k_x\in\mathbb{R}^+)}{\hat{N}(k_x,0)} = (\hat{f}_i^{(k_x,0)}\,\hat{u}_i^{(-k_x,0)} + \text{c.c.}) = 2\,\text{Real}\{\hat{f}_i^{(k_x,0)}\,\hat{u}_i^{(-k_x,0)}\}, \tag{A2c}$$

where c.c. represents complex conjugate terms; $\mathbb{R}$ refers to real numbers in Appendices A and B.

From the dyadic interactions in the wavenumber space, $\hat{f}_i^{(k_x,k_y)}$ could be expressed as

$$\begin{aligned}\hat{f}_i^{(k_x,k_y)} = &-\sum_{s_x,s_y\in\mathbb{R}^+}\left(\hat{u}_j^{(k_x-s_x,k_y-s_y)}\,\widehat{\frac{\partial u_i}{\partial x_j}}^{(s_x,s_y)} + \hat{u}_j^{(k_x+s_x,k_y+s_y)}\,\widehat{\frac{\partial u_i}{\partial x_j}}^{(-s_x,-s_y)}\right.\\ &\left.+\,\hat{u}_j^{(k_x+s_x,k_y-s_y)}\,\widehat{\frac{\partial u_i}{\partial x_j}}^{(-s_x,s_y)} + \hat{u}_j^{(k_x-s_x,k_y+s_y)}\,\widehat{\frac{\partial u_i}{\partial x_j}}^{(s_x,-s_y)}\right)\\ &-\sum_{b\in\mathbb{R}^+}\left(\hat{u}_j^{(k_x,k_y-s_y)}\,\widehat{\frac{\partial u_i}{\partial x_j}}^{(0,s_y)} + \hat{u}_j^{(k_x,k_y+s_y)}\,\widehat{\frac{\partial u_i}{\partial x_j}}^{(0,-s_y)}\right)\\ &-\sum_{a\in\mathbb{R}^+}\left(\hat{u}_j^{(k_x-s_x,k_y)}\,\widehat{\frac{\partial u_i}{\partial x_j}}^{(s_x,0)} + \hat{u}_j^{(k_x+s_x,k_y)}\,\widehat{\frac{\partial u_i}{\partial x_j}}^{(-s_x,0)}\right).\end{aligned} \tag{A3}$$

Substitute (A3) into (A2*a*), (A2*b*) and (A2*c*). The mode-to-mode nonlinear transfer between two modes for nine different cases is summarised here:

$$\begin{aligned}&\hat{M}_{(s_x,s_y)(k_x,k_y)}\\ &= -2\,\text{Real}\left\{\hat{u}_j^{(k_x-s_x,k_y-s_y)}\,\widehat{\frac{\partial u_i}{\partial x_j}}^{(s_x,s_y)}\,\hat{u}_i^{(-k_x,-k_y)} + \hat{u}_j^{(k_x+s_x,k_y+s_y)}\,\widehat{\frac{\partial u_i}{\partial x_j}}^{(-s_x,-s_y)}\,\hat{u}_i^{(-k_x,-k_y)}\right.\\ &\quad+\,\hat{u}_j^{(k_x+s_x,k_y-s_y)}\,\widehat{\frac{\partial u_i}{\partial x_j}}^{(-s_x,s_y)}\,\hat{u}_i^{(-k_x,-k_y)} + \hat{u}_j^{(k_x-s_x,k_y+s_y)}\,\widehat{\frac{\partial u_i}{\partial x_j}}^{(s_x,-s_y)}\,\hat{u}_i^{(-k_x,-k_y)}\\ &\quad+\,\hat{u}_j^{(-k_x-s_x,k_y-s_y)}\,\widehat{\frac{\partial u_i}{\partial x_j}}^{(s_x,s_y)}\,\hat{u}_i^{(k_x,-k_y)} + \hat{u}_j^{(-k_x+s_x,k_y+s_y)}\,\widehat{\frac{\partial u_i}{\partial x_j}}^{(-s_x,-s_y)}\,\hat{u}_i^{(k_x,-k_y)}\\ &\quad\left.+\,\hat{u}_j^{(-k_x+s_x,k_y-s_y)}\,\widehat{\frac{\partial u_i}{\partial x_j}}^{(-s_x,s_y)}\,\hat{u}_i^{(k_x,-k_y)} + \hat{u}_j^{(-k_x-s_x,k_y+s_y)}\,\widehat{\frac{\partial u_i}{\partial x_j}}^{(s_x,-s_y)}\,\hat{u}_i^{(k_x,-k_y)}\right\},\end{aligned} \tag{A4a}$$

$$\hat{M}_{(0,s_y)(k_x,k_y)} = -2\,\mathrm{Real}\left\{\hat{u}_j^{(k_x,k_y-s_y)}\,\widehat{\frac{\partial u_i}{\partial x_j}}^{(0,s_y)}\,\hat{u}_i^{(-k_x,-k_y)} + \hat{u}_j^{(k_x,k_y+s_y)}\,\widehat{\frac{\partial u_i}{\partial x_j}}^{(0,-s_y)}\,\hat{u}_i^{(-k_x,-k_y)}\right.$$
$$\left. + \hat{u}_j^{(-k_x,k_y-s_y)}\,\widehat{\frac{\partial u_i}{\partial x_j}}^{(0,s_y)}\,\hat{u}_i^{(k_x,-k_y)} + \hat{u}_j^{(-k_x,k_y+s_y)}\,\widehat{\frac{\partial u_i}{\partial x_j}}^{(0,-s_y)}\,\hat{u}_i^{(k_x,-k_y)}\right\}, \tag{A4b}$$

$$\hat{M}_{(s_x,0)(k_x,k_y)} = -2\,\mathrm{Real}\left\{\hat{u}_j^{(k_x-s_x,k_y)}\,\widehat{\frac{\partial u_i}{\partial x_j}}^{(s_x,0)}\,\hat{u}_i^{(-k_x,-k_y)} + \hat{u}_j^{(k_x+s_x,k_y)}\,\widehat{\frac{\partial u_i}{\partial x_j}}^{(-s_x,0)}\,\hat{u}_i^{(-k_x,-k_y)}\right.$$
$$\left. + \hat{u}_j^{(-k_x-s_x,k_y)}\,\widehat{\frac{\partial u_i}{\partial x_j}}^{(s_x,0)}\,\hat{u}_i^{(k_x,-k_y)} + \hat{u}_j^{(-k_x+s_x,k_y)}\,\widehat{\frac{\partial u_i}{\partial x_j}}^{(-s_x,0)}\,\hat{u}_i^{(k_x,-k_y)}\right\}, \tag{A4c}$$

$$\hat{M}_{(s_x,s_y)(0,k_y)} = -2\,\mathrm{Real}\left\{\hat{u}_j^{(-s_x,k_y-s_y)}\,\widehat{\frac{\partial u_i}{\partial x_j}}^{(s_x,s_y)}\,\hat{u}_i^{(0,-k_y)} + \hat{u}_j^{(s_x,k_y+s_y)}\,\widehat{\frac{\partial u_i}{\partial x_j}}^{(-s_x,-s_y)}\,\hat{u}_i^{(0,-k_y)}\right.$$
$$\left. + \hat{u}_j^{(s_x,k_y-s_y)}\,\widehat{\frac{\partial u_i}{\partial x_j}}^{(-s_x,s_y)}\,\hat{u}_i^{(0,-k_y)} + \hat{u}_j^{(-s_x,k_y+s_y)}\,\widehat{\frac{\partial u_i}{\partial x_j}}^{(s_x,-s_y)}\,\hat{u}_i^{(0,-k_y)}\right\}, \tag{A4d}$$

$$\hat{M}_{(0,s_y)(0,k_y)} = -2\,\mathrm{Real}\left\{\hat{u}_j^{(0,k_y-s_y)}\,\widehat{\frac{\partial u_i}{\partial x_j}}^{(0,s_y)}\,\hat{u}_i^{(0,-k_y)} + \hat{u}_j^{(0,k_y+s_y)}\,\widehat{\frac{\partial u_i}{\partial x_j}}^{(0,-s_y)}\,\hat{u}_i^{(0,-k_y)}\right\}, \tag{A4e}$$

$$\hat{M}_{(s_x,0)(0,k_y)} = -2\,\mathrm{Real}\left\{\hat{u}_j^{(-s_x,k_y)}\,\widehat{\frac{\partial u_i}{\partial x_j}}^{(s_x,0)}\,\hat{u}_i^{(0,-k_y)} + \hat{u}_j^{(s_x,k_y)}\,\widehat{\frac{\partial u_i}{\partial x_j}}^{(-s_x,0)}\,\hat{u}_i^{(0,-k_y)}\right\}, \tag{A4f}$$

$$\hat{M}_{(s_x,s_y)(k_x,0)} = -2\,\mathrm{Real}\left\{\hat{u}_j^{(k_x-s_x,-s_y)}\,\widehat{\frac{\partial u_i}{\partial x_j}}^{(s_x,s_y)}\,\hat{u}_i^{(-k_x,0)} + \hat{u}_j^{(k_x+s_x,s_y)}\,\widehat{\frac{\partial u_i}{\partial x_j}}^{(-s_x,-s_y)}\,\hat{u}_i^{(-k_x,0)}\right.$$
$$\left. + \hat{u}_j^{(k_x+s_x,-s_y)}\,\widehat{\frac{\partial u_i}{\partial x_j}}^{(-s_x,s_y)}\,\hat{u}_i^{(-k_x,0)} + \hat{u}_j^{(k_x-s_x,s_y)}\,\widehat{\frac{\partial u_i}{\partial x_j}}^{(s_x,-s_y)}\,\hat{u}_i^{(-k_x,0)}\right\}, \tag{A4g}$$

$$\hat{M}_{(0,s_y)(k_x,0)} = -2\,\mathrm{Real}\left\{\hat{u}_j^{(k_x,-s_y)}\,\widehat{\frac{\partial u_i}{\partial x_j}}^{(0,s_y)}\,\hat{u}_i^{(-k_x,0)} + \hat{u}_j^{(k_x,s_y)}\,\widehat{\frac{\partial u_i}{\partial x_j}}^{(0,-s_y)}\,\hat{u}_i^{(-k_x,0)}\right\}, \tag{A4h}$$

$$\hat{M}_{(s_x,s_y)(k_x,0)} = -2\,\mathrm{Real}\left\{\hat{u}_j^{(k_x-s_x,0)}\,\widehat{\frac{\partial u_i}{\partial x_j}}^{(s_x,0)}\,\hat{u}_i^{(-k_x,0)} + \hat{u}_j^{(k_x+s_x,0)}\,\widehat{\frac{\partial u_i}{\partial x_j}}^{(-s_x,0)}\,\hat{u}_i^{(-k_x,0)}\right\}. \tag{A4i}$$

Appendix B. Proof of $\hat{M}_{(s_x,s_y)(k_x,k_y)} = -\hat{M}_{(k_x,k_y)(s_x,s_y)}$

Note that $\hat{M}_{(s_x,s_y)(k_x,k_y)} = -\hat{M}_{(k_x,k_y)(s_x,s_y)}$ is satisfied only for wall-normal integrated $\hat{M}$. Two identities described below are used.

First, for three complex variables a, b and c, we have $\mathrm{Real}\{abc\} = \mathrm{Real}\{a^*b^*c^*\}$.

Second, for any set of triadic interaction, there exists a relationship that involves swapping the Fourier modes between the second and third terms:

$$-\int \hat{u}_j^{(k_x-s_x,k_y-s_y)}\,\widehat{\frac{\partial u_i}{\partial x_j}}^{(s_x,s_y)}\,\hat{u}_i^{(-k_x,-k_y)}\,\mathrm{d}z=\int \hat{u}_j^{(k_x-s_x,k_y-s_y)}\,\widehat{\frac{\partial u_i}{\partial x_j}}^{(-k_x,-k_y)}\,\hat{u}_i^{(s_x,s_y)}\,\mathrm{d}z. \tag{B1}$$

Proof. We have

$$\begin{aligned}
&\int \hat{u}_j^{(k_x-s_x,k_y-s_y)}\,\widehat{\frac{\partial u_i}{\partial x_j}}^{(s_x,s_y)}\,\hat{u}_i^{(-k_x,-k_y)}\,\mathrm{d}z+\int \hat{u}_j^{(k_x-s_x,k_y-s_y)}\,\widehat{\frac{\partial u_i}{\partial x_j}}^{(-k_x,-k_y)}\,\hat{u}_i^{(s_x,s_y)}\,\mathrm{d}z\\
&=\int \hat{u}_j^{(k_x-s_x,k_y-s_y)}\,\frac{\partial \hat{u}_i^{(s_x,s_y)}\hat{u}_i^{(-k_x,-k_y)}}{\partial x_j}\,\mathrm{d}z\\
&=\int\left(\hat{u}_j^{(k_x-s_x,k_y-s_y)}\,\frac{\partial \hat{u}_i^{(s_x,s_y)}\hat{u}_i^{(-k_x,-k_y)}}{\partial x_j}+\frac{\partial \hat{u}_j^{(k_x-s_x,k_y-s_y)}}{\partial x_j}\,\hat{u}_i^{(s_x,s_y)}\,\hat{u}_i^{(-k_x,-k_y)}\right)\mathrm{d}z\\
&=\int\frac{\partial(\hat{u}_j^{(k_x-s_x,k_y-s_y)}\hat{u}_i^{(s_x,s_y)}\hat{u}_i^{(-k_x,-k_y)})}{\partial x_j}\,\mathrm{d}z\\
&=\hat{u}_j^{(k_x-s_x,k_y-s_y)}\,\hat{u}_i^{(s_x,s_y)}\,\hat{u}_i^{(-k_x,-k_y)}\big|_{-1}^{1}\\
&=0.
\end{aligned} \tag{B2}$$

We use the continuity equation and the boundary conditions at the walls.

We consider three different cases. For each case, we list the terms in $\hat{M}_{(s_x,s_y)(k_x,k_y)}$ in the left-hand column, and the terms in $\hat{M}_{(k_x,k_y)(s_x,s_y)}$ in the right-hand column. Then we compare the columns. For simplicity, we use Fourier modes to represent the terms. For example, $(k_x-s_x,k_y-s_y)(s_x,s_y)(-k_x,-k_y)$ means the term $\hat{u}_j^{(k_x-s_x,k_y-s_y)}\,(\partial\hat{u}_i/\partial x_j)^{(s_x,s_y)}\,\hat{u}_i^{(-k_x,-k_y)}$. The first identity indicates $(k_x-s_x,k_y-s_y)(s_x,s_y)(-k_x,-k_y)=(s_x-k_x,s_y-k_y)(-s_x,-s_y)(k_x,k_y)$, and the second identity indicates $(k_x-s_x,k_y-s_y)(s_x,s_y)(-k_x,-k_y)=-(k_x-s_x,k_y-s_y)(-k_x,-k_y)(s_x,s_y)$.

(i) For $k_x,k_y,s_x,s_y\in\mathbb{R}^+$, according to (A4*a*):

$$\left.\begin{array}{ll}
\hat{M}_{(s_x,s_y)(k_x,k_y)} & \hat{M}_{(k_x,k_y)(s_x,s_y)}\\
①(k_x-s_x,k_y-s_y)(s_x,s_y)(-k_x,-k_y) & -①(s_x-k_x,s_y-k_y)(k_x,k_y)(-s_x,-s_y)\\
②(k_x+s_x,k_y+s_y)(-s_x,-s_y)(-k_x,-k_y) & -②(s_x+k_x,s_y+k_y)(-k_x,-k_y)(-s_x,-s_y)\\
③(k_x+s_x,k_y-s_y)(-s_x,s_y)(-k_x,-k_y) & -⑤(s_x+k_x,s_y-k_y)(-k_x,k_y)(-s_x,-s_y)\\
④(k_x-s_x,k_y+s_y)(s_x,-s_y)(-k_x,-k_y) & -⑥(s_x-k_x,s_y+k_y)(k_x,-k_y)(-s_x,-s_y)\\
⑤(-k_x-s_x,k_y-s_y)(s_x,s_y)(k_x,-k_y) & -③(-s_x-k_x,s_y-k_y)(k_x,k_y)(s_x,-s_y)\\
⑥(-k_x+s_x,k_y+s_y)(-s_x,-s_y)(k_x,-k_y) & -④(-s_x+k_x,s_y+k_y)(-k_x,-k_y)(s_x,-s_y)\\
⑦(-k_x+s_x,k_y-s_y)(-s_x,s_y)(k_x,-k_y) & -⑦(-s_x+k_x,s_y-k_y)(-k_x,-k_y)(s_x,-s_y)\\
⑧(-k_x-s_x,k_y+s_y)(s_x,-s_y)(k_x,-k_y) & -⑧(-s_x-k_x,s_y+k_y)(k_x,-k_y)(s_x,-s_y).
\end{array}\right\} \tag{B3}$$

(ii) For $k_x = 0$, k_y, s_x, $s_y \in \mathbb{R}^+$, according to (A4*d*):

$$\left.\begin{array}{ll} \hat{M}_{(s_x,s_y)(0,k_y)} & \hat{M}_{(0,k_y)(s_x,s_y)} \\ ①(-s_x, k_y - s_y)(s_x, s_y)(0, -k_y) & -①(s_x, s_y - k_y)(0, k_y)(-s_x, -s_y) \\ ②(s_x, k_y + s_y)(-s_x, -s_y)(0, -k_y) & -②(s_x, s_y + k_y)(0, -k_y)(-s_x, -s_y) \\ ③(s_x, k_y - s_y)(-s_x, s_y)(0, -k_y) & -③(-s_x, s_y - k_y)(0, k_y)(s_x, -s_y) \\ ④(-s_x, k_y + s_y)(s_x, -s_y)(0, -k_y) & -④(-s_x, s_y + k_y)(0, -k_y)(s_x, -s_y). \end{array}\right\} \tag{B4}$$

Terms $\hat{M}_{(s_x,s_y)(k_x,0)}$ and $\hat{M}_{(k_x,0)(s_x,s_y)}$ could be listed similarly.

(iii) For k_x, $a = 0$, k_y, $s_y \in \mathbb{R}^+$, according to (A4*e*):

$$\left.\begin{array}{ll} \hat{M}_{(0,s_y)(0,k_y)} & \hat{M}_{(0,k_y)(0,s_y)} \\ ①(0, k_y - s_y)(0, s_y)(0, -k_y) & -①(0, s_y - k_y)(0, k_y)(0, -s_y) \\ ②(0, k_y + s_y)(0, -s_y)(0, -k_y) & -②(0, s_y + k_y)(0, -k_y)(0, -s_y). \end{array}\right\} \tag{B5}$$

Terms $\hat{M}_{(s_x,0)(k_x,0)}$, $\hat{M}_{(k_x,0)(s_x,0)}$, $\hat{M}_{(s_x,0)(0,k_y)}$, $\hat{M}_{(0,k_y)(s_x,0)}$ could be listed similarly.

Combining these three cases, we prove that the nonlinear energy transfer from mode (s_x, s_y) to mode (k_x, k_y) equals the opposite of the nonlinear energy transfer from mode (k_x, k_y) to mode (s_x, s_y):

$$\hat{M}_{(s_x,s_y)(k_x,k_y)} = -\hat{M}_{(k_x,k_y)(s_x,s_y)}, \quad k_x, k_y, s_x, s_y \in \{\mathbb{R}^+ \cup 0\}. \tag{B6}$$

In addition, there is no nonlinear energy transfer from one mode to itself. This could be proved by setting $s_x = k_x$ and $s_y = k_y$ in (B6):

$$\hat{M}_{(k_x,k_y)(k_x,k_y)} = 0. \tag{B7}$$

Properties (B6) and (B7) are for wall-normal integrated $\hat{M}$.

References

Alexakis, A., Mininni, P.D. & Pouquet, A. 2005 Imprint of large-scale flows on turbulence. *Phys. Rev. Lett.* **95** (26), 264503.

Anderson, B.W. & Domaradzki, J.A. 2012 A subgrid-scale model for large-eddy simulation based on the physics of interscale energy transfer in turbulence. *Phys. Fluids* **24** (6), 065104.

Bae, H.J., Lozano-Duran, A. & McKeon, B.J. 2021 Nonlinear mechanism of the self-sustaining process in the buffer and logarithmic layer of wall-bounded flows. *J. Fluid Mech.* **914**, A3.

Blackwelder, R.F. & Eckelmann, H. 1979 Streamwise vortices associated with the bursting phenomenon. *J. Fluid Mech.* **94** (3), 577–594.

Brasseur, J.G. & Wei, C.-H. 1994 Interscale dynamics and local isotropy in high Reynolds number turbulence within triadic interactions. *Phys. Fluids* **6** (2), 842–870.

Cho, M., Hwang, Y. & Choi, H. 2018 Scale interactions and spectral energy transfer in turbulent channel flow. *J. Fluid Mech.* **854**, 474–504.

Chung, D., Monty, J.P. & Ooi, A. 2014 An idealised assessment of Townsend's outer-layer similarity hypothesis for wall turbulence. *J. Fluid Mech.* **742**, R3.

Cimarelli, A. & De Angelis, E. 2014 The physics of energy transfer toward improved subgrid-scale models. *Phys. Fluids* **26** (5), 055103.

Cimarelli, A., De Angelis, E. & Casciola, C.M. 2013 Paths of energy in turbulent channel flows. *J. Fluid Mech.* **715**, 436–451.

Cimarelli, A., De Angelis, E., Jimenez, J. & Casciola, C.M. 2016 Cascades and wall-normal fluxes in turbulent channel flows. *J. Fluid Mech.* **796**, 417–436.

Domaradzki, J.A. 1992 Nonlocal triad interactions and the dissipation range of isotropic turbulence. *Phys. Fluids* A **4** (9), 2037–2045.

DOMARADZKI, J.A., LIU, W., HÄRTEL, C. & KLEISER, L. 1994 Energy transfer in numerically simulated wall-bounded turbulent flows. *Phys. Fluids* **6** (4), 1583–1599.
DOMARADZKI, J.A. & ROGALLO, R.S. 1990 Local energy transfer and nonlocal interactions in homogeneous, isotropic turbulence. *Phys. Fluids* A **2** (3), 413–426.
DUNN, D.C. & MORRISON, J.F. 2003 Anisotropy and energy flux in wall turbulence. *J. Fluid Mech.* **491**, 353–378.
ERTESVÅG, I.S. & MAGNUSSEN, B.F. 2000 The eddy dissipation turbulence energy cascade model. *Combust. Sci. Technol.* **159** (1), 213–235.
GERMANO, M., PIOMELLI, U., MOIN, P. & CABOT, W.H. 1991 A dynamic subgrid-scale eddy viscosity model. *Phys. Fluids* A **3** (7), 1760–1765.
GÜRCAN, Ö.D., LI, Y. & MOREL, P. 2020 Turbulence as a network of Fourier modes. *Mathematics* **8** (4), 530.
HAMILTON, J.M., KIM, J. & WALEFFE, F. 1995 Regeneration mechanisms of near-wall turbulence structures. *J. Fluid Mech.* **287**, 317–348.
HÄRTEL, C., KLEISER, L., UNGER, F. & FRIEDRICH, R. 1994 Subgrid-scale energy transfer in the near-wall region of turbulent flows. *Phys. Fluids* **6** (9), 3130–3143.
HASSELMANN, K., MUNK, W. & MACDONALD, G.J.F. 1963 Bispectra of ocean waves. In *M. Rosenblatt Time Series Analysis.* John Wiley.
HUTCHINS, N. & MARUSIC, I. 2007 Evidence of very long meandering features in the logarithmic region of turbulent boundary layers. *J. Fluid Mech.* **579**, 1–28.
HWANG, Y. & BENGANA, Y. 2016 Self-sustaining process of minimal attached eddies in turbulent channel flow. *J. Fluid Mech.* **795**, 708–738.
HWANG, Y. & COSSU, C. 2010 Amplification of coherent streaks in the turbulent Couette flow: an input–output analysis at low Reynolds number. *J. Fluid Mech.* **643**, 333–348.
JIMÉNEZ, J. 2018 Coherent structures in wall-bounded turbulence. *J. Fluid Mech.* **842**, P1.
JIN, B., SYMON, S. & ILLINGWORTH, S.J. 2021 Energy transfer mechanisms and resolvent analysis in the cylinder wake. *Phys. Rev. Fluids* **6** (2), 024702.
JOVANOVIĆ, M.R. & BAMIEH, B. 2005 Componentwise energy amplification in channel flows. *J. Fluid Mech.* **534**, 145–183.
KARBAN, U., MARTINI, E., CAVALIERI, A.V.G. & JORDAN, P. 2023 Modal decomposition of nonlinear interactions in wall turbulence. arXiv:2301.01078.
KOLMOGOROV, A.N. 1941 The local structure of turbulence in incompressible viscous fluid for very large Reynolds numbers. *C. R. Acad. Sci. URSS* **30**, 301–305.
LEE, M. & MOSER, R.D. 2019 Spectral analysis of the budget equation in turbulent channel flows at high Reynolds number. *J. Fluid Mech.* **860**, 886–938.
LOZANO-DURÁN, A., BAE, H.J. & ENCINAR, M.P. 2020 Causality of energy-containing eddies in wall turbulence. *J. Fluid Mech.* **882**, A2.
MCKEON, B.J. 2017 The engine behind (wall) turbulence: perspectives on scale interactions. *J. Fluid Mech.* **817**, P1.
MENEVEAU, C. & SREENIVASAN, K.R. 1991 The multifractal nature of turbulent energy dissipation. *J. Fluid Mech.* **224**, 429–484.
MOIN, P. & KIM, J. 1982 Numerical investigation of turbulent channel flow. *J. Fluid Mech.* **118**, 341–377.
MOSER, R.D., KIM, J. & MANSOUR, N.N. 1999 Direct numerical simulation of turbulent channel flow up to $Re_\tau = 590$. *Phys. Fluids* **11** (4), 943–945.
PIOMELLI, U., CABOT, W.H., MOIN, P. & LEE, S. 1991 Subgrid-scale backscatter in turbulent and transitional flows. *Phys. Fluids* A **3** (7), 1766–1771.
POPE, S.B. 2000 *Turbulent Flows*. Cambridge University Press.
PUJALS, G., GARCÍA-VILLALBA, M., COSSU, C. & DEPARDON, S. 2009 A note on optimal transient growth in turbulent channel flows. *Phys. Fluids* **21** (1), 015109.
REDDY, S.C. & HENNINGSON, D.S. 1993 Energy growth in viscous channel flows. *J. Fluid Mech.* **252**, 209–238.
RICHARDSON, L.F. 1922 *Weather Prediction by Numerical Process*. Cambridge University Press.
DE SALIS YOUNG, J., HAO, Z. & GARCIA-MAYORAL, R. 2024 Inter-scale causality relations in wall turbulence. *J. Phys.: Conf. Ser.* **2753**, 012019.
SCHMID, P.J. & HENNINGSON, D.S. 2001 *Stability and Transition in Shear Flows*. Springer.
SMAGORINSKY, J. 1963 General circulation experiments with the primitive equations: I. The basic experiment. *Mon. Weath. Rev.* **91** (3), 99–164.
SMYTH, W.D. 1992 Spectral transfers in two-dimensional anisotropic flow. *Phys. Fluids* A **4** (2), 340–349.
SYMON, S., ILLINGWORTH, S.J. & MARUSIC, I. 2021 Energy transfer in turbulent channel flows and implications for resolvent modelling. *J. Fluid Mech.* **911**, A3.

TENNEKES, H. & LUMLEY, J.L. 1972 *A First Course in Turbulence*. MIT Press.
WALEFFE, F. 1992 The nature of triad interactions in homogeneous turbulence. *Phys. Fluids* A **4** (2), 350–363.
WALEFFE, F. 1997 On a self-sustaining process in shear flows. *Phys. Fluids* **9** (4), 883–900.
WEBBER, G.A., HANDLER, R.A. & SIROVICH, L. 2002 Energy dynamics in a turbulent channel flow using the Karhunen–Loéve approach. *Intl J. Numer. Meth. Fluids* **40** (11), 1381–1400.